

Gaussianity*

Enrique Martínez-González
Instituto de Física de Cantabria (CSIC-UC),
Av. Los Castros s/n, 39005 Santander, Spain
email: martinez@ifca.unican.es
(Dated: 17th April 2008)

In this chapter we review the present status of the Gaussianity studies of the CMB anisotropies, including physical effects producing non-Gaussianity, methods to test it and observational constraints.

Contents

I. Introduction	1
II. The isotropic Gaussian random field (IGRF)	2
A. Definition	2
B. Properties	3
III. Physical effects producing deviations from the standard IGRF	6
A. Secondary anisotropies	6
B. Non-standard models of the early universe	9
1. Non-standard inflationary models	9
2. Topological defects	10
C. Non-standard geometry and topology	10
D. Primordial magnetic fields	11
IV. Methods to test Gaussianity	11
V. Constraints from observations	13
VI. WMAP anomalies	14
A. North-south asymmetry	14
B. Alignment of the low multipoles	16
C. The cold spot	16
D. Alignment and signed-intensity of local structures	16
E. Low variance	17
F. Cosmological consequences	17
1. Bianchi model	17
2. The cold spot texture	18
VII. Concluding remarks and future perspectives	18
References	19

I. INTRODUCTION

The study of the CMB temperature and polarization anisotropy has had an essential role in establishing the standard cosmological model: a flat Λ CDM model composed of baryonic matter ($\approx 4\%$), dark matter ($\approx 24\%$) and dark energy ($\approx 72\%$), with nearly scale-invariant adiabatic fluctuations in the energy-density. The information extracted from the CMB to derive the cosmological model has been mostly based on the CMB anisotropy power spectrum. However, much more information is still waiting to be extracted from the statistics of the CMB beyond the second-order moment.

* Chapter of the book “Cosmic Microwave Background: from quantum fluctuations to the present universe”, IAC Winter School 2007.

The study of the Gaussianity of the CMB anisotropies has become in recent years a very relevant topic in the CMB field. The main reason for that is the availability of high sensitivity and high resolution maps provided by the new generations of CMB experiments, with which the Gaussian character of the anisotropies predicted by the standard inflationary paradigm can be tested at a high accuracy. CMB anisotropies form an ideal data set for testing the Gaussianity of the primordial energy-density fluctuations since the dominant physical effects producing the anisotropies involves just linear physics, and Gaussianity is preserved under linear transformations. Another approach to test it is by studying the large scale structure of the universe as described by the galaxy distribution. The density perturbations in the linear regime should also be a good representation of the initial conditions. However, galaxy formation is a very non-linear process involving complex physical effects which very much complicate the analysis.

Different models of the early universe have been proposed to naturally account for the early stages of its history and, thus, not to have to rely on ad hoc initial conditions. They are based on different theories, like string theory or M theory, and include or not an inflationary phase (an example of the latter being the Ekpyrotic cosmology [91]). Most of those models predict very specific properties about the probability distribution of the CMB anisotropies, which in many cases imply deviations from Gaussianity with amplitudes within reach of present or near future experiments. Some of those models are already constrained by present data and many more are expected to be disproved in the coming years, specially with the launch of the Planck satellite at the end of 2008 (or beginning of 2009).

The analysis of the angular distribution of the CMB anisotropies is a formidable task with profound consequences on our understanding of the universe. Before any meaningful result can be achieved, it is, however, crucial to control at a high level of precision all possible systematics that can be introduced by the experiment and the pipeline process used to reduce the data. On the other hand, there are several Galactic and extragalactic emissions in the microwave band which blur the CMB signal. Disentangling the cosmic signal from the others is also crucial and requires a very good knowledge of the astrophysical emissions. A lot of observational and theoretical effort has been dedicated to that aim in recent years. Below we summarize the present status of the most important aspects of the analysis of Gaussianity and the results achieved.

II. THE ISOTROPIC GAUSSIAN RANDOM FIELD (IGRF)

One of the most robust predictions of the standard inflationary model is that the CMB anisotropies should be well represented by an isotropic Gaussian random field (IGRF) on the celestial sphere. This is a very powerful prediction to test the standard model. There are many statistical quantities for a IGRF that can be derived analytically, which greatly facilitates the Gaussianity test of the CMB data. However, a disadvantage may come from the central limit theorem that implies that the sum of several independent non-Gaussian distributions tends to a more Gaussian one. As we will see below, this complicates the Gaussianity analysis since the observational data is composed of several contributions which can be either intrinsic or extrinsic to the CMB anisotropies.

A. Definition

A random field defined on a given support is said to be Gaussian if for any N points of the support x_1, \dots, x_n the values of the random field y_1, \dots, y_n follow a multinormal distribution

$$f(y_1, \dots, y_n) = \frac{1}{(2\pi)^{n/2} |M|^{1/2}} \exp \left(-\frac{1}{2} \sum_{ij} (y_i - \langle y_i \rangle) M_{ij}^{-1} (y_j - \langle y_j \rangle) \right) \quad (1)$$

where M is the covariance matrix defined as $M_{ij} = \langle (y_i - \langle y_i \rangle)(y_j - \langle y_j \rangle) \rangle$. Thus the n-pdf (probability density function), and also all the moments, is given in terms of just the first two moments.

In the case of the temperature anisotropies of the CMB the mean value is set to zero, and thus the standard model predicts a Gaussian pdf characterized by only the second moment. The support is in this case the 2D sphere. Thus the temperature anisotropies can be expanded in terms of the spherical harmonic coefficients,

$$\Delta(\mathbf{n}) \equiv \frac{\Delta T}{T}(\mathbf{n}) = \sum_{lm} a_{lm} Y_{lm}(\mathbf{n}) \quad (2)$$

where $Y_{lm}(\mathbf{n})$ are the spherical harmonic functions for direction \mathbf{n} and a_{lm} are the spherical harmonic coefficients which for the standard model are Gaussian distributed .

If the field is isotropic then the two-point correlation function only depends on the modulus of the difference of the two directions. In harmonics space, isotropy translates in that the harmonic coefficients are uncorrelated

$$\langle a_{lm} a_{l'm'}^* \rangle = C_l \delta_{ll'} \delta_{mm'} \quad (3)$$

where δ_{ij} is the Kronecker delta. C_l is the temperature power spectrum which for a realization can be estimated as $(2l+1)^{-1} \sum_l |a_{lm}|^2$.

B. Properties

The IGRF is one of the best studied random fields and many of its properties have been thoroughly analysed. One of the most remarkable properties is that the expectation of any even combination of the field $\Delta(\mathbf{n})$ can be given in terms of the second moment, the 2-point correlation function, and the expectation of any odd combination is zero; i.e. the n-point correlation functions for n odd are zero. The same property translates to the spherical harmonics space where the expectation of even combinations of the coefficients a_{lm} can be expressed in terms of the power spectrum C_l and the expectation of odd combinations, e.g. the bispectrum, is zero. More generally, a very useful characteristic of a IGRF is that the expectations of many statistical quantities can be calculated (semi)analytically. This is the case for the morphological descriptors, number, shape and correlation of peaks (maxima), scalars on the sphere, ...

The Minkowski functionals are useful descriptors of the morphology of point sets or smoothed fields in spaces with arbitrary dimension d (see e.g. [1]). As stated in [138], under a few simple requirements any morphological descriptor can be written as a linear combination of $d+1$ Minkowski functionals. For the sphere they are therefore 3; namely, total length of the contour $C(\nu)$ of the excursion set, total area $A(\nu)$ of the excursion set and the genus $G(\nu)$ above a threshold ν . Their average value per unit area for a IGRF can be simply given by

$$\langle C(\nu) \rangle = \frac{1}{8\theta_c} \exp\left(-\frac{\nu^2}{2}\right) , \quad (4)$$

$$\langle A(\nu) \rangle = \frac{1}{2} - \frac{2}{\sqrt{\pi}} \int_0^{\nu/\sqrt{2}} \exp(-x^2) dx , \quad (5)$$

$$\langle G(\nu) \rangle = \frac{1}{(2\pi)^{3/2} \theta_c^2} \nu \exp\left(-\frac{\nu^2}{2}\right) , \quad (6)$$

where $\theta_c = \left(-\frac{C(0)}{C''(0)}\right)^{1/2}$ is the coherence angle of the random field which is defined by the ratio of the two-point correlation function $C(\theta)$ to its second derivative at zero lag (see Fig. 1).

Properties of peaks in a 2D IGRF have been studied by [110], [23] and [7]. The local description of a peak involves the second derivative of the field along the two principal directions. The curvature radii are defined in the usual way from the second derivative of the temperature anisotropies Δ at the position of the maximum: $R_1 = [-\Delta_1''(max)/2\sigma_0]^{-1/2}$ $R_2 = [-\Delta_2''(max)/2\sigma_0]^{-1/2}$, where σ_0 is the anisotropy rms and Δ_i'' is the second derivative along the principal direction i . The two invariant quantities, Gaussian curvature κ and eccentricity ϵ can be constructed from them:

$$\kappa = \frac{1}{R_1 R_2} , \quad \epsilon = \left[1 - \left(\frac{R_2}{R_1}\right)^2\right]^{1/2} . \quad (7)$$

It is straightforward to obtain the number of peaks on the celestial sphere $N(\kappa, \epsilon, \nu) d\kappa d\epsilon d\nu$ with Gaussian curvature, eccentricity and threshold between $(\kappa, \kappa + d\kappa)$, $(\epsilon, \epsilon + d\epsilon)$ and $(\nu, \nu + d\nu)$, in terms of the two spectral parameters γ and θ_* that characterize the cosmological model:

$$\gamma = \frac{\sigma_1^2}{\sigma_0 \sigma_2} , \quad \theta_* = 2^{1/2} \frac{\sigma_1}{\sigma_2} , \quad (8)$$

$$\sigma_0^2 = C(0) , \quad \sigma_1^2 = -2C''(0) , \quad \sigma_2^2 = \frac{8}{3} C^{(iv)}(0) . \quad (9)$$

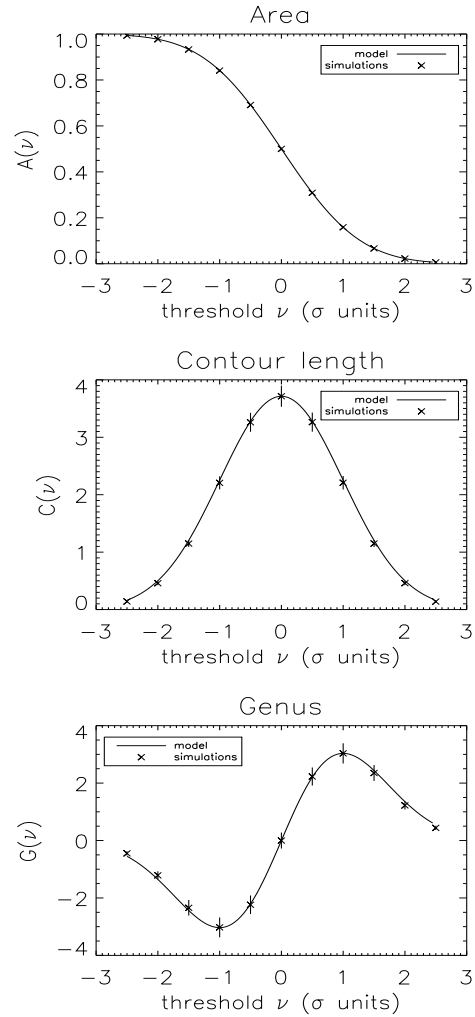


FIG. 1: Expected value of the Minkowski functionals for an IGRF obtained from eq. 4, eq. 5, eq. 6. Also plotted are the average values (asterisk) and error bars of the Minkowski functionals obtained with 1000 Gaussian simulations. Taken from [46].

The number of peaks above a threshold ν , $N(\nu)$, can be calculated from the previous differential quantity by integrating over the whole parameter space for κ and ϵ and over the interval (ν, ∞) for ν :

$$\begin{aligned}
 N(\nu) = & N_T \left(\frac{6}{\pi} \right)^{1/2} \exp(-\nu^2/2) \left\{ \gamma^2(\nu^2 - 1) \left[1 - \frac{1}{2} \operatorname{erfc}(\gamma\nu s) \right] + \right. \\
 & + \nu\gamma(1 - \gamma^2) \frac{s}{\pi^{1/2}} \exp(-\gamma^2\nu^2 s^2) + \\
 & \left. + t \left[1 - \frac{1}{2} \operatorname{erfc}(\gamma\nu s t) \right] \exp(-\gamma^2\nu^2 t^2) \right\}, \tag{10}
 \end{aligned}$$

where

$$s = [2(1 - \gamma^2)]^{-1/2} \quad , \quad t = (3 - 2\gamma^2)^{-1/2} \quad , \quad (11)$$

and $N_T = (3^{1/2}\theta_*^2)^{-1}$ is the total number of peaks on the whole celestial sphere.

Another interesting quantity is the distribution of the curvature of the peaks. The pdf of peaks with inverse of the Gaussian curvature $L \equiv \kappa^{-1}$ between $(L, L + dL)$ above the threshold ν , $p(L)$, can be also obtained from $N(\kappa, \epsilon, \nu) d\kappa d\epsilon d\nu$:

$$p(L) = \left(\frac{6}{\pi}\right)^{1/2} (2\gamma\theta_c^2)^4 t L^{-5} \exp[(2\gamma\theta_c^2)^2 L^{-2}] \int_{\nu}^{\infty} d\nu \exp(-3t^2\nu^2/2) \operatorname{erfc}\left[\frac{s}{t}(2\gamma\theta_c^2 L^{-1} - \gamma\nu t^2)\right] . \quad (12)$$

The distribution of excentricities can be calculated in a similar manner. The pdf of peaks with eccentricity between $(\epsilon, \epsilon + d\epsilon)$ above a threshold ν , $p(\epsilon)$, can be obtained after a straightforward calculation:

$$p(\epsilon) = \frac{32\sqrt{6}}{\pi} \epsilon^3 \frac{1 - \epsilon^2}{(2 - \epsilon^2)^5} \int_{\nu}^{\infty} d\nu \exp(\nu^2/2) \left\{ (H\pi)^{1/2} \exp(-G) \left[1 - \operatorname{erfc}(H^{1/2}\gamma\nu s)/2 \right] \times \right. \\ \left. [3H^2(1 - \gamma^2)^2 + 6H^3\gamma^2(1 - \gamma^2)\nu^2 + (H\gamma\nu)^4] + \right. \\ \left. \exp(-s^2\gamma^2\nu^2) s [5H^3\gamma(1 - \gamma^2)^2\nu + H^4(\gamma\nu)^3(1 - \gamma^2)] \right\} , \quad (13)$$

where $H = (2 - \epsilon^2)^2 / [(3 - 2\gamma^2)\epsilon^4 + 4(1 - \epsilon^2)]$ and $G = H(\gamma\nu\epsilon^2)^2 / (2 - \epsilon^2)^2$.

Scalar quantities can be constructed from the derivatives of the CMB field on the sphere. A single scalar can be constructed in terms of the ordinary derivative of the field $\Delta_{,i}$. Only two independent scalars can be obtained from the second covariant derivatives on the sphere, $\Delta_{;ij}$. Following [122], many scalar quantities can be defined from the first and second derivatives of the field, associated to the Hessian matrix, the distortion, the gradient and the curvature. However, all except three are correlated. For testing Gaussianity, it is convenient to use normalized scalars for which the dependence of the scalars on the power spectrum has been removed. Here, as example, we focus on three independent normalized scalars, namely the Laplacian, the fractional anisotropy and the square of the modulus of the gradient. The first two scalars have been proved to be very efficient as detectors of non-Gaussianity [123]. The third scalar, the square of the modulus of the gradient, is the only scalar from the list given in that paper which is independent from all the others. It depends only on the first derivatives of the field. The Laplacian and the fractional anisotropy depend only on second derivatives and can be defined in terms of the eigenvalues λ_1, λ_2 , of the negative Hessian matrix \mathbf{A} of the field: $\mathbf{A} = (-T_{;ij})$. The eigenvalues, i.e. the negative second derivatives along the two principal directions, can be written as a function of the covariant second derivatives of the field $\Delta(\mathbf{n})$:

$$\lambda_1 = -\frac{1}{2} \left[\left(\Delta^i_i \right) - \sqrt{\left(\Delta^i_i \right)^2 - 2 \left(\Delta^i_i \Delta^j_j - \Delta^i_j \Delta^i_j \right)} \right] , \quad (14)$$

$$\lambda_2 = -\frac{1}{2} \left[\left(\Delta^i_i \right) + \sqrt{\left(\Delta^i_i \right)^2 - 2 \left(\Delta^i_i \Delta^j_j - \Delta^i_j \Delta^i_j \right)} \right] . \quad (15)$$

We will assume $\lambda_1 \geq \lambda_2$. Considering the values of λ_1 and λ_2 , three types of points can be distinguished (see e.g. [55]: hill (both positive), lake (both negative) and saddle (one positive and one negative)

The normalized Laplacian, or trace of the Hessian matrix, $\bar{\lambda}_+$, is defined in terms of the eigenvalues as:

$$\bar{\lambda}_+ = \frac{\lambda_1 + \lambda_2}{\sigma_2} , \quad -\infty < \bar{\lambda}_+ < \infty . \quad (16)$$

Since the Laplacian is given by linear transformations of the CMB temperature fluctuation field Δ , if the field is Gaussian then its 1-point pdf is also Gaussian:

$$p(\bar{\lambda}_+) = \frac{1}{\sqrt{2\pi}} \exp\left(-\frac{\bar{\lambda}_+^2}{2}\right) \quad (17)$$

The fractional anisotropy [15] has been used in other fields like in the analysis of medical images. The normalized quantity \bar{f}_a is defined as:

$$\bar{f}_a = \frac{1}{\sqrt{2}} \frac{\bar{\lambda}_1^2 - \bar{\lambda}_2^2}{\sqrt{\lambda_1^2 + \lambda_2^2}} \quad (18)$$

where $\bar{\lambda}_1$ and $\bar{\lambda}_2$ are the normalized eigenvalues given by:

$$\begin{pmatrix} \bar{\lambda}_1 \\ \bar{\lambda}_2 \end{pmatrix} = \frac{1}{2} \begin{pmatrix} \frac{1}{\sigma_2} + \frac{1}{\sqrt{\sigma_2^2 - 2\sigma_1^2}} & \frac{1}{\sigma_2} - \frac{1}{\sqrt{\sigma_2^2 - 2\sigma_1^2}} \\ \frac{1}{\sigma_2} - \frac{1}{\sqrt{\sigma_2^2 - 2\sigma_1^2}} & \frac{1}{\sigma_2} + \frac{1}{\sqrt{\sigma_2^2 - 2\sigma_1^2}} \end{pmatrix} \begin{pmatrix} \lambda_1 \\ \lambda_2 \end{pmatrix}. \quad (19)$$

The pdf of the normalized fractional anisotropy is given by:

$$p(\bar{f}_a) = \frac{2\bar{f}_a}{(1 - \bar{f}_a^2)^{1/2}(1 + \bar{f}_a^2)^{3/2}}, \quad 0 < \bar{f}_a < 1. \quad (20)$$

The normalized square of the modulus of the gradient \bar{g} , which depends only on the first derivatives of the field, is defined as:

$$\bar{g} = \frac{|\nabla\Delta|^2}{\sigma_1^2} = \frac{\Delta_{,i}\Delta_{,i}}{\sigma_1^2}, \quad (21)$$

where σ_1^2 is the dispersion of the unnormalized square of the modulus of the gradient and accounts for the normalization factor. In terms of the derivatives of the field with respect to the spherical coordinates (θ, ϕ) , \bar{g} takes the form:

$$\bar{g} = \frac{1}{\sigma_1^2} \left[\left(\frac{\partial\Delta}{\partial\theta} \right)^2 + \frac{1}{\sin^2\theta} \left(\frac{\partial\Delta}{\partial\phi} \right)^2 \right]. \quad (22)$$

Taking into account that the square of the gradient modulus is given by the addition of two independent squared Gaussian variables, its pdf follows a χ_2^2 distribution. Since we consider the normalized quantity \bar{g} , then its mean and dispersion are equal to one and its distribution takes the simple form:

$$p(\bar{g}) = \exp(-\bar{g}), \quad 0 < \bar{g} < \infty. \quad (23)$$

The pdfs of the three normalized scalars can be seen in Fig. 2. Maps of the same scalars for a random realization of a IGRF are shown in Fig. 3.

III. PHYSICAL EFFECTS PRODUCING DEVIATIONS FROM THE STANDARD IGRF

There are a number of physical effects which may produce deviations from the standard IGRF. They are normally related to secondary anisotropies produced by photon scattering, gravitational effects generated by the non-linear evolution of the matter density, variations from standard inflation in the early universe, topological defects, non-standard geometry and topology of the universe or primordial magnetic fields. Below we summarize some relevant aspects of the most studied effects.

A. Secondary anisotropies

On the last scattering surface CMB anisotropies are generated via the gravitational potential (Sachs-Wolfe effect, [136]) and the physics of the baryon-photon plasma. These anisotropies are usually referred to as *primary anisotropies*. After matter-radiation decoupling when the temperature drops below $\approx 3000K$, new anisotropies are generated during the trip made by the CMB photons to reach us. These *secondary anisotropies* can be originated via the gravitational redshift suffered by the photons when crossing the gravitational potentials produced by the large-scale matter distribution, or by the scattering of the microwave photons with the ionised matter after the reionization epoch ($z \lesssim 10$). The gravitational potential can produce two types of effect: the gravitational redshift suffered by the photons when they cross the varying potential wells formed by the matter evolution (Rees-Sciama effect, [115, 131]), and the lensing effect produced by the same gravitational potentials which bends their trajectory (see e.g. Bartelmann

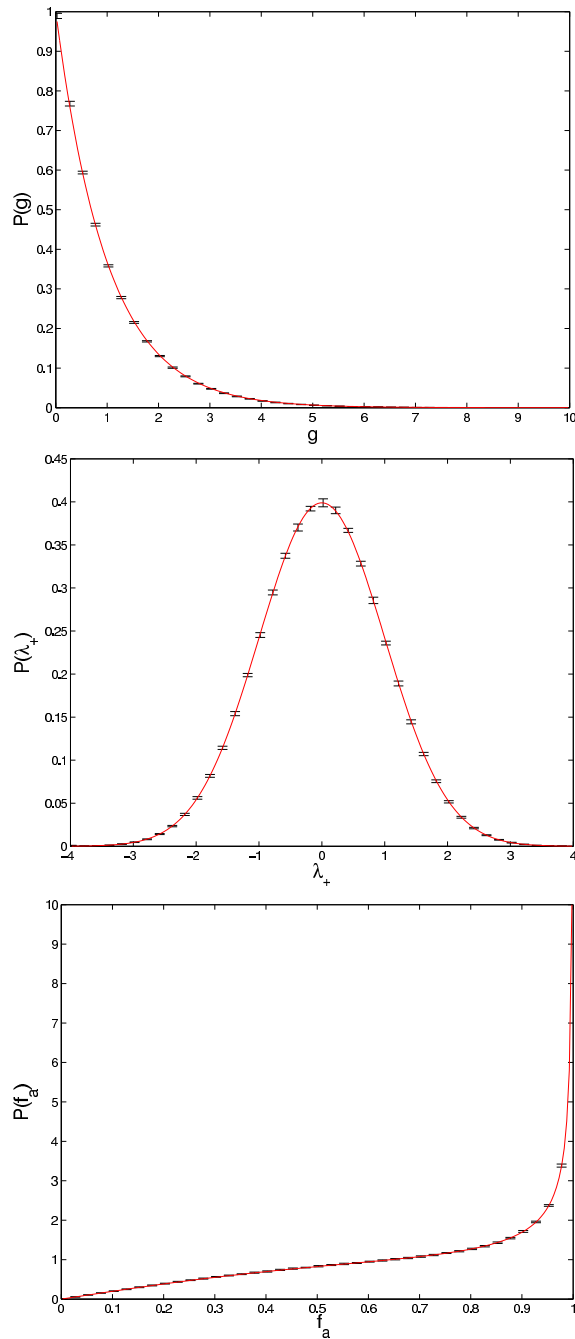


FIG. 2: Pdfs of the three normalized scalars described in the text: the Laplacian (eq. 17), the fractional anisotropy (eq. 20) and the square of the modulus of the gradient (eq. 23). The average values and error bars of 1000 IGRF simulations are also represented. From [122].

and Schneider 2001 for a review). The CMB power spectrum produced by the Rees-Sciama effect is subdominant on all angular scales [81, 137], and the expected 3-point correlations have an amplitude much below the cosmic variance [121]. The lensing effect produces a smoothing of the acoustic peaks in the CMB power spectrum [117, 139]. It also induces high-order correlations in the CMB temperature and polarization fields [79].

The scattering of the CMB photons with the ionised medium produces a randomisation of the directions of the rescattered photons, implying a suppression of the primary CMB anisotropies whose resulting power spectrum depends on the Thompson optical depth τ as $\exp(-2\tau)$. In addition, new anisotropies are generated by the scattering with the free electrons moving along the line of sight which produces a Doppler effect. This effect is strongly suppressed

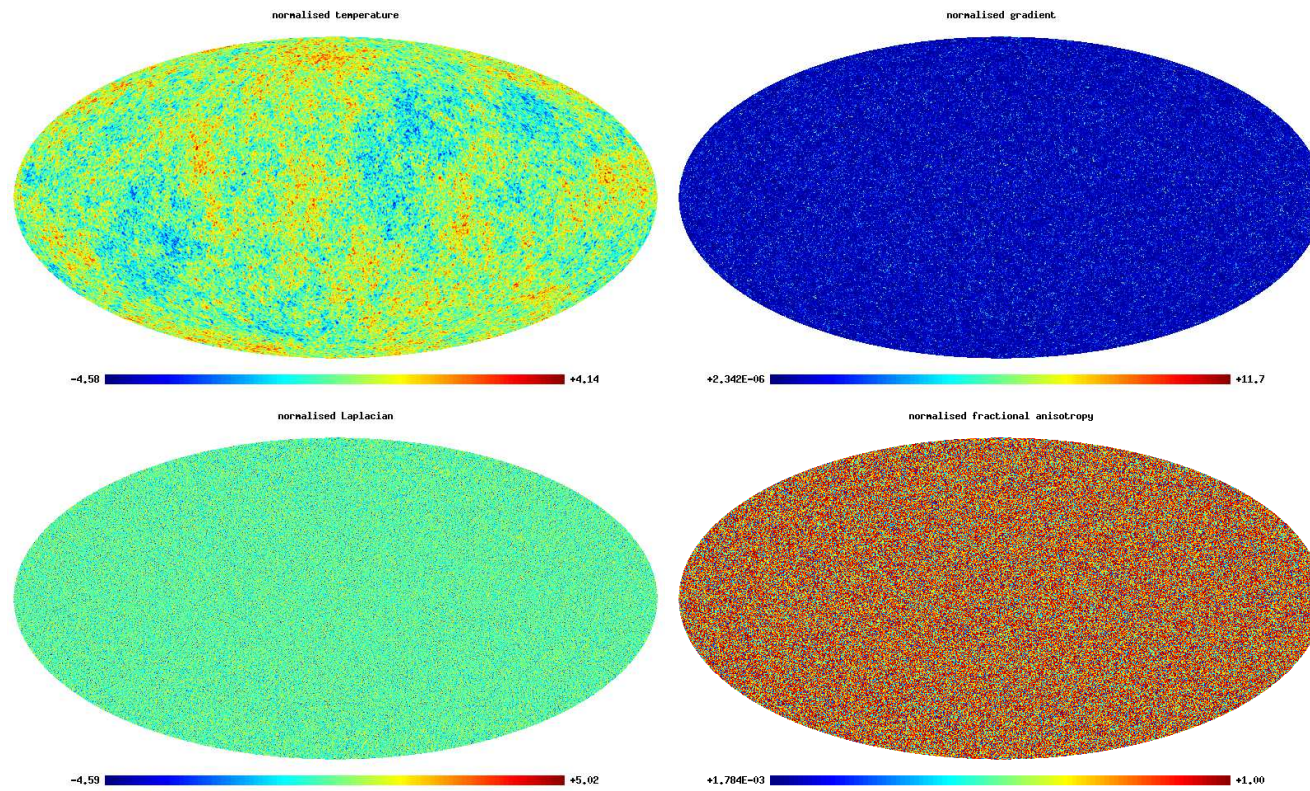


FIG. 3: Maps of the three normalized scalars described in the text and of the corresponding normalized temperature for a realization of the IGRF. From [122].

due to the cancellation of velocities along the line of sight. However the Doppler effect can survive cancellation if it is modulated by either density or ionization fluctuations. Its amplitude is given by:

$$\frac{\Delta T}{T} = -\sigma_T \int dt e^{-\tau(\theta,t)} n_e(\theta,t) v_r(\theta,t) . \quad (24)$$

In this formula σ_T is the Thompson cross-section, n_e the electron density and v_r the line of sight velocity of the electrons. n_e can be further expressed as $n_e(\theta,t) = \bar{n}_e(t)[1 + \delta(\theta,t) + \delta_i(\theta,t)]$ where $\bar{n}_e(t)$ is the mean electron density, δ the density fluctuation and δ_i the ionisation fraction. Two second order effects generating secondary anisotropies appear in this formula. The first one is the Doppler effect modulated by the density variation and known as *Ostriker and Vishniac effect* in the linear regime [127, 153]. The second effect is the Doppler effect modulated by the ionisation fraction and is usually referred to as *patchy reionization* (see e.g. [4]). Since they are of second order, both effects produce non-Gaussian perturbations in the CMB. However, their amplitude is much smaller than the thermal and kinetic *Sunyaev-Zeldovich effects (SZ)* [144] generated in the non-linear regime at lower redshifts and produced by the scattering of hot, ionised gas associated to collapsed structures. In addition to temperature anisotropies, due to the primary quadrupole moment reionisation also produces polarisation.

For more details about secondary anisotropies the reader is referred to e.g. [81] and [5].

B. Non-standard models of the early universe

1. Non-standard inflationary models

In the standard, single field, slow roll inflationary model, the dominant linear effects in the evolution of density fluctuations preserve the initial Gaussian distribution produced by the quantum fluctuations of the inflaton. On the contrary, second-order effects perturb the original Gaussianity of the fluctuations, although resulting in a negligible effect in the standard model. In non-standard inflationary models, primordial non-Gaussianity should be added to the second-order effects associated to the evolution of density fluctuations after inflation finishes. In any case, it is common to characterize phenomenologically the deviations from Gaussianity by introducing the f_{NL} parameter in the gravitational potential [95]:

$$\phi = \phi_L + f_{NL} \phi_L^2 , \quad (25)$$

where ϕ_L is the gravitational potential at the linear order and it is distributed following a Gaussian random field. In general the *non-linear couplig parameter* f_{NL} is a function of the distance vectors and the product is really a convolution. However, an effective f_{NL} which accounts for those complexities can still be used. A detailed study of the values of f_{NL} for several non-standard inflationary models, including multi-field inflation, the curvaton scenario, inhomogeneous reheating and the Dirac-Born-Infeld (DBI) inflation inspired by string theory, can be found in [13] (see also [120] in this volume). Here it is worth noticing that sometimes the specific f_{NL} parameter given by eq. 25 is called the *local* non-linear coupling parameter f_{NL}^{local} , referring to the fact that ϕ is obtained from ϕ_L at the same position in space. In addition to f_{NL}^{local} which contains mainly information of the squeezed configurations (those with two large and similar wave vectors and the other small), the *equilateral* non-linear coupling parameter f_{NL}^{equil} is used to characterize equilateral configurations of the bispectrum for which the lengths of the three wave vectors are equal in Fourier space. The two non-linear coupling parameters suppose a fair representation of a large class of models. For instance, f_{NL}^{local} can be generated in curvaton and reheating scenarios whereas f_{NL}^{equil} can be produced in DBI inflation within the context of String theory.

In the standard single-field slow-roll inflation the effective f_{NL} is dominated by second-order gravitational corrections leading to values of order unity. These low values require very sensitive measurements to be detected and are not even within reach of the Planck mission. Non-standard inflationary models generally predict larger values, some of them already constrained by WMAP. A positive detection of $f_{NL} \gtrsim 10$ would rule out the standard inflationary models.

For an ideal experiment with white noise, no foreground residuals and no Galactic and point source mask, it has been shown that the optimal estimator for f_{NL} is based on a bispectrum test constructed from a cubic combination of appropriately filtered temperature and polarization maps [40, 98, 157]. An extension to this estimator to deal with data under realistic experimental conditions has been made by [158]. Several observational constraints on f_{NL} have been derived from different experiments. The first ones were obtained with COBE-DMR [31, 96]. Further constraints have been derived with other experiments like VSA [140], BOOMERANG [51] and Archeops [46, 47]. However, the best limits have been derived with the various releases of the WMAP data [97, 99, 142] representing an improvement of at least an order of magnitude over previous ones (see below).

2. Topological defects

In standard theories of particle physics the fundamental forces of nature unify progressively when the energy scale exceeds certain thresholds. These unified theories imply that the universe went through several phase transitions during the early stages of its evolution. At energies above 10^2GeV , the electromagnetism and the weak nuclear force are merged into the electroweak force. At higher energies of the order of 10^{15}GeV it is believed that the electroweak force unifies with the strong nuclear force, a process usually called Grand Unified Theory (GUT). At even higher energies it is speculated that it is possible to merge gravity with the other three interactions.

Unified theories are based on symmetry. When the symmetry is broken spontaneously via the Higgs mechanism, topological defects generically appear [92] (for a more pedagogical discussion about topological defects see [149]). Depending on the dimensionality of the symmetry which is broken, a type of topological defect is formed. When a discrete symmetry is broken domain walls form, in a two-dimensional symmetry breaking cosmic strings appear, monopoles form when the symmetry breaking is three-dimensional and textures appear when it is in four or more dimensions. In the 1980s topological defects were considered as an alternative scenario to inflationary quantum fluctuations for the process of structure formation. CMB observations showed that the former scenario could only play a subdominant role as the source of cosmic structure. Moreover, due to the catastrophic effects that the presence of domain walls and monopoles would have on our universe only the existence of cosmic strings and textures is usually considered.

A lot of effort has been made to study the cosmological consequences of cosmic strings. It is generally believed that the best strategy to detect them is by searching for their imprint on the CMB maps. The non-Gaussian character of the density field of strings produce line discontinuities in the CMB anisotropies at arcmin angular scales as a consequence of the metric deformation around the strings (the Kaiser-Stebins effect [89]). However, at larger angular scales a Gaussian distribution emerge from the central limit theorem.

Cosmic textures were first studied in detail by [147]. They are much more diffuse than the other defects which are localized at a point (monopole), on a line (cosmic string) or a surface (domain wall). Contrary to the others, they are unstable and consist of twisted configurations of fields which collapse and unwind. Each texture creates a time-varying gravitational potential which produces red- or blue-shift to the CMB photons passing through such a region. Thus, textures generate hot and cold spots on the CMB anisotropy maps whose amplitude is set by the symmetry breaking energy scale. The shape of the spots is approximately spherically symmetric and an approximated analytical formula has been derived by [148]. Recently, a very cold spot detected in the WMAP temperature map has been found to be consistent with the effect produced by a texture [44]. If confirmed, this result will have outstanding consequences in our understanding of the universe (see Sec. VIF 2 for more details on this finding).

C. Non-standard geometry and topology

The geometry of the observable universe is believed to be well approximated on large scales by a Friedmann-Lemaitre-Robertson-Walker (FLRW) metric characterized by a homogeneous and isotropic space-time. Support for the homogeneity of the universe is provided by the largest surveys of the galaxy distribution (e.g. SDSS DR6 [3], 2dFGRS [36]) and by the smallness of the CMB temperature fluctuations. The cosmological principle, stating that the universe is homogeneous and isotropic on large scales, follows from those observations and the assumption that we are not located at a special place in the universe (the Copernican principle).

However, recent observations of the CMB as measured by the WMAP satellite might question the cosmological principle. They are the large scale power asymmetry found between the two hemispheres of a reference frame close to that of the ecliptic one [59, 72], the planarity and alignment of the low multipoles [49, 104], the non-Gaussian cold spot present at scales of $\approx 10^\circ$ [42, 150] and the alignment of local structures also at similar scales [151, 155] (see Sec. VI for more details). These results may imply the existence of privileged directions in the CMB map and thus motivates the study of alternatives to the standard FLRW metric.

An interesting class of alternative models is that for which the metric is homogeneous but anisotropic. They are known as Bianchi models and are classified according to their space-time properties. Their predictions for the CMB anisotropy were studied in [10]. Since the signatures left by those models appear on large angular scales, they have been already constrained by the COBE-DMR experiment data [27, 93, 116]. One particularly interesting case is Bianchi VII_h which experiences anisotropic expansion and global rotation. These two properties produce a characteristic pattern in the CMB in the form of a spiral pattern and spots. This model has been recently used to account for some of the large scale WMAP anomalies mentioned above [24, 85, 86, 87] (see Sec. VIF 1 for more details). An important problem with this model comparison approach is that the CMB anisotropies are not computed in a self-consistent way but are assumed to be the sum of two independent components: an isotropic one produced by the energy-density

fluctuations which is assumed to be the same than for the FLRW model, and an anisotropic component which is the deterministic effect produced by the anisotropic model.

A different source of anisotropic features in the CMB sky is the global topology of the universe. The local character of the General Theory of Relativity does not theoretically constrain it. If the topology of the universe is non-trivial (i.e. multiconnected, meaning that there is not a unique way to connect two points by geodesics) then CMB photons originated from the same location on the last scattering surface can be observed in different directions. This effect manifests itself in the CMB sky as anisotropic patterns, correlated (matched) circles [39] or, more generically, as deviations from a IGRF (for a discussion on different topologies and tests developed to detect them see the reviews by [103] and [108]). An additional consequence of a multiconnected universe is the lack of fluctuations in the CMB above the wavelength corresponding to the size of the universe. This property has led to several authors to suggest that the low quadrupole and the alignment of the low multipoles measured by WMAP might be an evidence of a non-trivial topology [41, 111]. Constraints on the topology of the universe started with the COBE-DMR data [48, 132, 133] and followed with the WMAP data [83, 101, 102, 126, 130]. All those analyses concluded that the WMAP data do not show any evidence of multiconnected universes.

D. Primordial magnetic fields

In recent years there has been an increasing interest in studying the consequences that the possible existence of primordial magnetic fields might have on the CMB. Magnetic fields of order of a few μG have been measured in a wide range of astrophysical structures, from individual galaxies [71] to galaxy clusters [100]. It is also widely believed that they are present in superclusters. Although the origin of those magnetic fields is still unclear and their existence does not necessarily imply a primordial origin, studying the interplay between magnetic fields and CMB is justified by the important consequences that it may have on the CMB temperature and polarization anisotropy, and also on the distortion of the blackbody spectrum (for reviews on this topic the reader is referred to [58, 67]). In particular, the presence of magnetic fields introduce non-Gaussianity in the CMB anisotropy since its amplitude depends on the square of the magnetic field intensity.

Two very different cases can be considered for the primordial magnetic field: a uniform field and a stochastic one. The former breaks the spatial isotropy of the background geometry by introducing shear through an anisotropic stress. This leads to the well known homogeneous and anisotropic Bianchi models [10]. Since those models also imply an anisotropic CMB field, a uniform magnetic field generates phase correlations between different a_{lm} . The uniform magnetic field has been constrained with the CMB quadrupole and also with the phase correlations, implying comparable constraints on the magnetic field intensity of a few nG [11, 33, 57].

The stochastic magnetic field is a more realistic scenario which can be generated during inflation. In this case the isotropy of the background geometry is preserved. Temperature and polarization anisotropies are generated through the vector and tensor modes associated to the magnetic field energy-momentum tensor. Allowed amplitudes of the magnetic field intensity of about several nG can produce a potentially observable B-mode polarization for nearly scale invariant spectra [109]. This signal could be distinguished from the one generated by the inflationary gravitational wave background by its non-Gaussian character. In addition Faraday rotation induces B-mode polarization from the ordinary E-mode with the characteristic ν^{-2} dependence.

Therefore, the presence of a primordial magnetic field can leave unambiguous inprints in the CMB anisotropy that would allow its identification with the sensitive data expected from the coming experiments.

IV. METHODS TO TEST GAUSSIANTY

Testing the Gaussianity of CMB data is not an easy task. In principle it consists in just proving the properties of the IGRF that we discussed in Sec. II B: isotropy and multinormality. The CMB data represent a single realization of the underlying random field which for the standard model is nearly Gaussian and isotropic. In practice the analysis is complicated by the characteristics of the experiment which need to be known very precisely: calibration uncertainties, instrumental noise (white and 1/f) which is normally anisotropic in pixel space depending on the scanning strategy, beam response (usually close to Gaussian), data processing, ... And by foreground contamination which demands certain previous cleaning operations in the data, requiring masking certain areas where the foregrounds are very intense and leaving some amount of residuals in the rest of the surveyed area. The result of cleaning depends on our a priori knowledge of the physical properties of the foregrounds and the component separation method used for their removal. These ingredients must be considered in the analysis by performing simulations accounting for them.

Unless one is interested in the compatibility of the data with a specific alternative model for which an optimal method may be found (as specific non-standard inflation, geometry or topology), there are infinite ways in which a

random field can deviate from the IGRF one. Methods to test Gaussianity can be classified by the type of property that they try to prove. Typical examples are cumulants and n-point correlation functions in real space (the former should vanish and the latter either vanish for the odd order or can be expressed in terms of 2-point correlation functions for the even order), moments in spherical harmonics space (bispectrum, trispectrum, ...), or moments in other spaces to which the data is transformed by linear operations which preserve Gaussianity: filters, wavelets, signal-to-noise eigenvectors, ... Other approaches may test different properties of the CMB random field, like the morphology of the data using the Minkowski Functionals or the geometry of the data using scalar quantities constructed by the first and second covariant derivatives as, for example, the local curvature (see Sec. IIB). These and other methods are described in more detail in [119] and [8] and references therein. As example of the typical statistical procedure followed in the analysis, below we focus on a few statistical methods which have been often used in the literature based on the Minkowski Functionals, bispectrum or wavelets.

As we have described in Sec. IIB, for the excursion set above a given threshold ν , there are three Minkowski Functionals on the sphere: total contour length $C(\nu)$, total area $A(\nu)$ and the genus $G(\nu)$ (see [138]). In the case of an IGRF their expected values follow simple analytical expressions as a function of ν (eqs. 4,5,6). However, simulations are needed to account for the experimental characteristics, basically noise, beam response and mask. As it can be shown with simulations, the 1-pdf for any Minkowski Functional at each ν follows a nice bell-shape distribution, implying the natural choice of a generalized χ^2 as the appropriate statistical test to be used in this case to combine all the information. More specifically, considering n_{th} different thresholds we can define a $3n_{th}$ vector \mathbf{v} ,

$$\mathbf{v} = (A(\nu_1), \dots, A(\nu_{n_{th}}), C(\nu_1), \dots, C(\nu_{n_{th}}), G(\nu_1), \dots, G(\nu_{n_{th}})) \quad . \quad (26)$$

The generalized χ^2 statistic to test the Gaussianity of a data map can be then constructed as

$$\chi^2 = \sum_{i,j=1}^{3n_{th}} (v_i - \langle v_i \rangle) C_{ij} (v_j - \langle v_j \rangle) \quad (27)$$

where $\langle \rangle$ is the expected value for the Gaussian case and C_{ij} is the covariance matrix, $C_{ij} = \langle v_i v_j \rangle - \langle v_i \rangle \langle v_j \rangle$, both of them usually constructed with simulations. For testing the compatibility of the data with a non-Gaussian model (e.g. a non-standard inflationary model characterized by the f_{NL} parameter) we simply have to use the corresponding expected value and covariance matrix for the Minkowski Functionals at different thresholds in eq. 27. If the deviations from Gaussianity are small (as in the case of the f_{NL} models with $f_{NL} \lesssim 1000$) the covariance matrix can be well approximated by the one of the Gaussian case. More information is added to the analysis by considering n_{res} different resolutions of a given data map. Including this extra information simply increases the vectors and covariance matrix present in the χ^2 expression to a dimension $3n_{th}n_{res}$. Examples of applications of this method to different data sets can be found in [97] for the 1-year WMAP data, [51] for the BOOMERanG 3-year data and [47] for the Archeops data. Recently, perturbative formulae of the Minkowski Functionals as a function of f_{NL} have been derived for the f_{NL} models [74]. The results of applying them to the 3-year WMAP data show constraints on f_{NL} very similar to the ones obtained with the optimal bispectrum [75].

Generically, non-standard models of inflation produce small deviations of Gaussianity which are more prominent in the 3-point correlation function or equivalently, its harmonic transform the bispectrum $B_{l_1 l_2 l_3}^{m_1 m_2 m_3} \equiv \langle a_{l_1 m_1} a_{l_2 m_2} a_{l_3 m_3} \rangle$. The trispectrum, the harmonic transform of the 4-point correlation function, can also play an important role in discriminating inflation models since some models do not produce any bispectra but produce significant trispectra, or produce similar amplitudes of the bispectra but very different trispectra (e.g. DBI inflation, [78], or New Ekpyrotic Cosmology, [26]). Here we briefly describe the bispectrum, for more details on it and the trispectrum see [94]. The average bispectrum, $B_{l_1 l_2 l_3}$, is the rotationally invariant third order moment of spherical harmonic coefficients and is given by the following expression (see [80] and [13] for more details on this and higher order moments):

$$B_{l_1 l_2 l_3} = \sum_{m_1 m_2 m_3} \begin{pmatrix} l_1 & l_2 & l_3 \\ m_1 & m_2 & m_3 \end{pmatrix} \langle a_{l_1 m_1} a_{l_2 m_2} a_{l_3 m_3} \rangle \quad , \quad (28)$$

where (...) is the Wigner-3j symbol. The bispectrum must satisfy the selection rules. Rotational invariance of the 3-point correlation function implies that the bispectrum can be written as

$$B_{l_1 l_2 l_3}^{m_1 m_2 m_3} = G_{l_1 l_2 l_3}^{m_1 m_2 m_3} b_{l_1 l_2 l_3} \quad , \quad (29)$$

where $G_{l_1 l_2 l_3}^{m_1 m_2 m_3}$ is the Gaunt factor and $b_{l_1 l_2 l_3}$ is a real symmetric function of l_1 , l_2 and l_3 called the *reduced bispectrum*. By substituting eq. 29 in eq. 28 it is straight forward to obtain the following relation between the

averaged bispectrum and the reduced bispectrum

$$B_{l_1 l_2 l_3} = \sqrt{\frac{(2l_1 + 1)(2l_2 + 1)(2l_3 + 1)}{4\pi}} \begin{pmatrix} l_1 & l_2 & l_3 \\ 0 & 0 & 0 \end{pmatrix} b_{l_1 l_2 l_3} . \quad (30)$$

Therefore under rotational invariance the reduced bispectrum contains all physical information of the bispectrum. In particular $b_{l_1 l_2 l_3}$ is fully identified by the inflationary models characterized by the non-linear coupling parameter f_{NL} . Thus these models can be optimally tested by using the averaged bispectrum. The computation of the full averaged bispectrum scales as $N_{pix}^{5/2}$, where N_{pix} is the number of pixels, and is already not feasible for the WMAP data. [98] solved this problem by constructing a cubic statistic, the KSW estimator, that combines the triangle configurations of the bispectrum optimally for determining f_{NL}^{local} , with its computation scaling as $N_{pix}^{3/2}$. The extension of this estimator to f_{NL}^{equil} , and also including polarization, has been made in [40] and [157]. The strongest constraints on the non-linear coupling parameter up to date have been obtained by applying the KSW estimator to the WMAP data (see next section).

Wavelets are compensated filters which allow one to extract information which is localized in both real and harmonics space. In particular wavelets may provide information on the position and scale of different features in astrophysical images. They can be more sensitive than classical methods (for a review on wavelets see [88] and for applications to the CMB see [152]). One example which has been used many times in cosmological applications is the Mexican hat wavelet defined as the Laplacian of a Gaussian function. For CMB analyses the extension of an Euclidean wavelet to the sphere can be made with an inverse stereographic projection [6]. By this procedure the spherical Mexican hat wavelet can be constructed preserving dilation and compensation [118], and was first applied to CMB analyses by [30] using COBE-DMR data. Also it can be made directional, i.e. sensitive not only to the scale but also to the orientation of a feature, by simply considering different widths along the two axes of the original 2-dimensional Gaussian.

A very useful property to study directional properties of structures in an image is the so called steerability. In general, a directional or non-axisymmetric filter is said to be *steerable* if any rotation about itself can be expressed as a finite linear combination of non-rotated basis filters. This concept has been recently extended to the sphere by [154]. An important consequence of the steerability property is that it makes the wavelet analysis very efficient computationally (see Sec. VID). An interesting spherical steerable wavelet is the second Gaussian derivative one which may be rotated in terms of three basis wavelets: the second derivative in direction x, the second derivative in direction y, and the cross-derivative. This wavelet provides information on the three local morphological measures of orientation, signed intensity (amplitude at the orientation which maximizes the absolute value of the coefficient) and elongation. It has been recently applied to the CMB analysis to test global isotropy and Gaussianity [151, 155, 156] (see Sec. VID).

V. CONSTRAINTS FROM OBSERVATIONS

Previously to any Gaussianity study, one major problem in the analysis of the observational data is the separation of the different Galactic and extragalactic components from the CMB itself. A key property to distinguish them is the frequency dependence of the specific emission in the microwave range. Thus, the intensity of the Galactic synchrotron and free-free emissions decreases with frequency as a power-law with approximated spectral indexes 3 and 2, respectively. On the contrary, the intensity of the Galactic thermal dust increases with frequency following approximately a grey-body spectrum with emissivity $\propto \nu^2$ and temperature $T_D \approx 10 - 20\text{K}$. Extragalactic sources emitting in the microwave band are typically radio galaxies and IR galaxies, with their emission dominating at frequencies $\lesssim 100\text{GHz}$ for the former (synchrotron-like) and at higher ones (dust-like) for the latter. An additional extragalactic emission comes from galaxy clusters through the SZ effect, as was discussed in Sec. III A. The spatial distribution of the different foregrounds is also very different from the CMB one, differing very much from that of an IGRF. Thus, the Galactic foreground emissions dominate at large angular scales with the power spectrum of fluctuations decaying approximately as $C_\ell \propto \ell^{-3}$. On the contrary the extragalactic foregrounds dominate at the smallest angular scales and appear as point sources for typical CMB experiments. (For more details on the properties of foregrounds see contributions by [53] and [129] to this volume). All these properties have to be exploited in order to best disentangle the foreground emissions from the CMB one. Indeed, the numerous component separation methods already developed take advantage of our knowledge of those foreground properties to obtain a clean CMB map (see [56] and [9] for further reading on this topic).

The Gaussianity of the CMB signal has been studied with data measured by many different experiments. The first systematic analysis was carried out with the all-sky COBE-DMR satellite [16, 141]. Other analyses were based on data covering a fraction of the sky and obtained from experiments onboard stratospheric balloons, like QMAP, MAXIMA, BOOMERanG or Archeops, and from ground-based ones like Saskatoon, QMASK or VSA. The result of most of those Gaussianity studies was a systematic compatibility with the standard IGRF. Deviations were also

claimed in a few cases which were later proved to be due to either systematics or an incomplete analysis. Upper limits on the f_{NL}^{local} parameter were derived of approximately a few thousands [31, 96]. For a more detailed discussion on those analyses see [119]. A significant improvement has been recently achieved with measurements by BOOMERanG and Archeops, lowering the upper limit to $f_{NL} \lesssim 1000$ at the 2σ c.l. [47, 51]. It is worth mentioning a deviation from the IGRF found in one of the VSA fields, the Corona Borealis supercluster [65, 134]. The deviation consists in a strong and resolved negative spot, of $\approx -250\mu\text{K}$ and angular size of ≈ 20 arcmin, which is not associated with any of the clusters of that supercluster. A SZ effect produced by a diffuse, extended warm/hot gas distribution has been suggested as a possible explanation [66]. This hypothesis, if confirmed, would be of relevance for providing the location of the missing baryons in the local universe.

The precision with which the Gaussianity of the CMB can be tested has been strongly improved with the quality data measured with the WMAP satellite [17, 76, 77]. The WMAP team has provided “cleaned” CMB maps at the Q, V and W frequency bands for the 5 year data collected by the experiment, and masks covering a region around the Galactic plane and a catalogue of radio sources where the foreground emission cannot be removed at the required sensitivity. By a noise-weighting combination of the cleaned maps at the cosmological frequencies and applying a conservative mask the WMAP team has performed a Gaussianity study of the data based on the Minkowski Functionals and the optimal bispectrum. For both quantities the 1, 3 and 5-year WMAP data releases have been found to be compatible with the IGRF [97, 99, 142]. Stringent limits have been also derived on the local and equilateral f_{NL} parameter using an optimal bispectrum-like quantity: $-9 < f_{NL}^{local} < 111$ and $-151 < f_{NL}^{equil} < 253$ at the 2σ c.l.

VI. WMAP ANOMALIES

The WMAP team found the WMAP data consistent with the IGRF using the Minkowski functionals and the bispectrum. Subsequently, many works have tested the Gaussianity of the WMAP data in many different ways. Some of them have found agreement with Gaussianity whereas others found significant deviations of the IGRF. Examples of the former are analyses based on 3-point correlation analysis [34, 64], integrated bispectrum [28], real space statistics [14] or isotropy analyses based on the Bipolar power spectrum [69, 70]. Examples of the latter are analyses based on phase correlations [35], the genus [128], isotropic wavelets [42, 125, 150], 1-pdf [124], isotropy analyses based on local n-point correlations [59], local curvature [73], multipole vectors [37, 38] or directional wavelets [112, 151, 155, 156]. However, some of the analyses have been performed on the whole sky internal linear combination (ILC) map [18] or similar maps (e.g. [145]) which is well known to suffer from Galactic contamination and, as stated by the WMAP team itself, should not be used for cosmological analyses. From here on, we will concentrate on the most relevant works based on WMAP maps where a certain region around the Galactic plane has been masked as well as several hundred of extragalactic sources. The deviations or “anomalies” reported have been detected using other statistical quantities different from the ones originally used by the WMAP team. They are the North-South asymmetry [59, 72], alignment of the low multipoles [49, 104], the cold spot [42, 44, 150], non-Gaussian features detected with directional wavelets [112, 113], alignment of CMB structures [151, 155], low variance [124]. Below we describe these anomalies and discuss several relevant aspects like significance, origin, etc.

A. North-south asymmetry

North-South asymmetries in ecliptic coordinates have been observed in the WMAP CMB maps using several local quantities: power spectrum and 2 and 3-point correlation functions [59, 61], Minkowski functionals [60], local power spectrum [54, 72], local bispectra [105] and local curvature [73]. Varying the coordinate system, a maximum asymmetry for the two hemispheres is obtained for a system whose north pole is lying at $(\theta, \phi) = (80^\circ, 57^\circ)$. This direction is close to the north ecliptic pole $(\theta, \phi) = (60^\circ, 96^\circ)$ (see Fig. 4). The result of all those works basically indicates a significant lack of power in the north ecliptic hemisphere compared to the south one. The asymmetry has been also confirmed by [19, 20] using a pair angular separation histogram method.

The asymmetry remains stable with respect to variations in the Galaxy cut and to the frequency band. Also a similar asymmetry is found in the COBE-DMR map with the axis of maximum asymmetry close to the one found in the WMAP data. Analyses of the possible foreground contamination and known systematics do not seem to be the cause of such asymmetry [59].

More recently, the asymmetry has been found again in the 3-year WMAP CMB map [62].

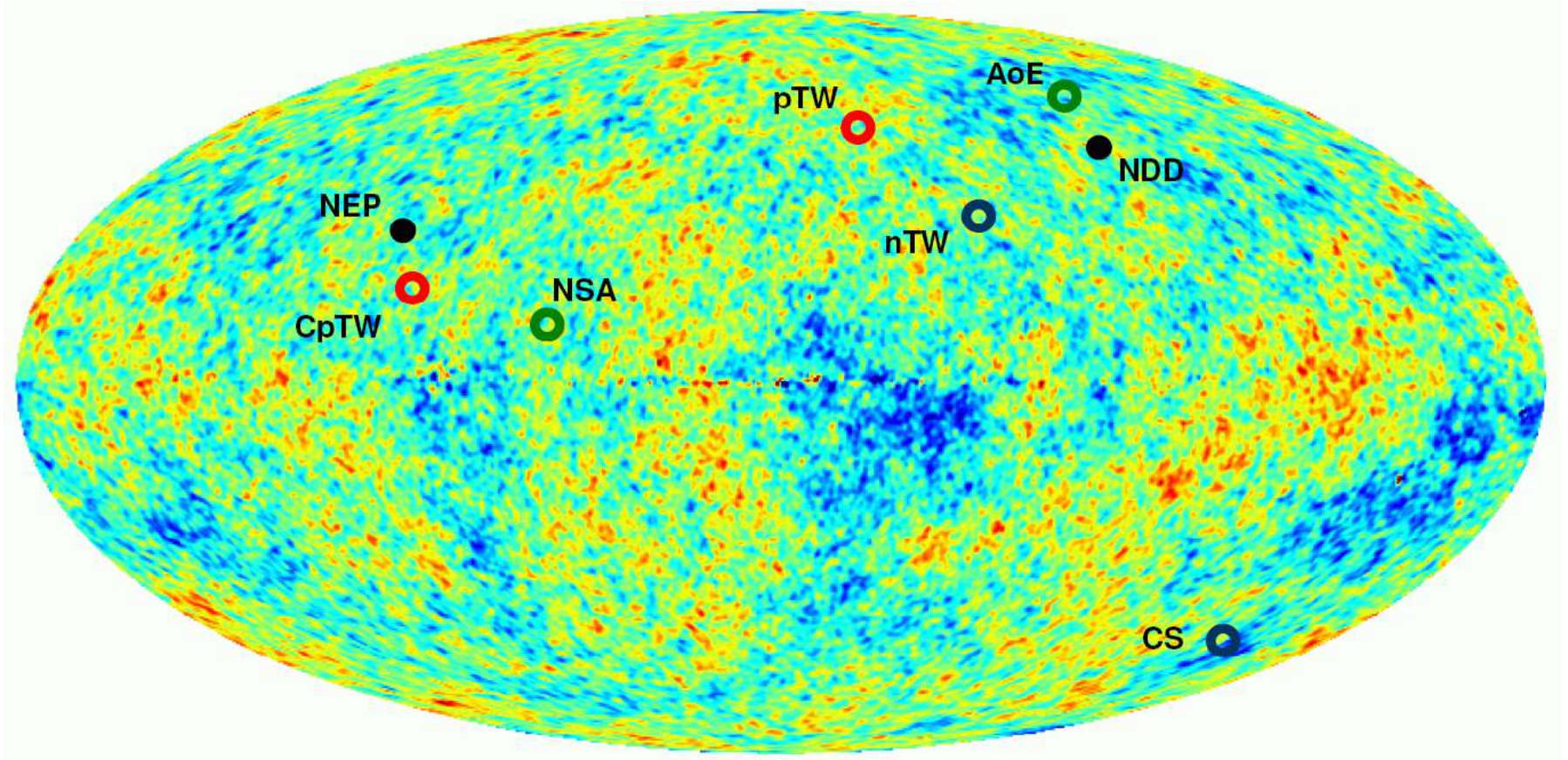


FIG. 4: Directions in the microwave sky derived from the anomalies found in WMAP data: northern direction of the North-South asymmetry (NSA), axis of evil (AoE), the cold spot (CS), cluster of positive total weights (CpTW), perpendicular axis to the positive total weights plane (pTW), perpendicular axis to the negative total weights plane (nTW). For reference the North ecliptic pole (NEP) and the northern direction of the CMB dipole (NDD) are also shown.

B. Alignment of the low multipoles

The lowest multipoles, especially $\ell = 2, 3$, of the WMAP data have been found to be anomalously planar and aligned [22, 37, 38, 49, 90, 143]. In Fig. 5 the quadrupole and octopole of the ILC map are shown. Both multipoles present maxima and minima following a planar shape, whose perpendicular axis points towards similar direction called axis of evil. The axes of the two multipoles are separated by $\approx 10^\circ$. The probability that the two directions are separated by that angle or less by chance is $\approx 1.5\%$. Further alignments have also been claimed for higher multipoles $\ell \leq 5$ [104] and $\ell = 6, 7$ [63]. The northern end of the alignment points towards $(\theta, \phi) = (30^\circ, 260^\circ)$, a direction close to the CMB dipole one whose northern end is at $(\theta, \phi) = (42^\circ, 264^\circ)$ (see Fig. 4).

A problem which appears when trying to estimate the low multipole components is that they are very much affected by the mask. Varying the mask produces significant changes in their amplitude estimates, especially for the quadrupole, implying consequently uncertainties in the determination of their axes. Detailed analyses of this effect tend to weaken the significance of the detection [50, 107].

C. The cold spot

A large and prominent cold spot has been observed in the WMAP data which is hard to explain within the standard inflationary scenario. It was detected with the SMHW as defined in [118]. The first evidence came from the kurtosis of the wavelet coefficients of the first-year data which showed an excess with respect to the Gaussian hypothesis at a wavelet scale of $\approx 4^\circ$ (corresponding to a structure size of $\approx 10^\circ$) [150]. A very cold spot at Galactic coordinates $(\theta, \phi) = (-57^\circ, 209^\circ)$ was identified as the possible source of the excess (see Fig. 6). An analysis of the area of the spots at different thresholds in the SMHW coefficient map at around 4° proved that indeed the cold spot had a very large area and was the source of the excess of the kurtosis [42].

The cold spot has been also shown to deviate from Gaussianity using the Max and Higher Criticism estimators [32, 42]. A study of the morphology of the spot with the elliptical MHW on the sphere has found an almost circular shape [43]. In the same paper the possible foreground contribution was considered in detail, concluding that contributions from the SZ effect and the Galaxy had to be negligible.

The cold spot has been also identified as the most prominent spot in the CMB sky using steerable wavelets [151]. In that work two other spots are identified as deviations from the IGRF three-year WMAP best fitting model. However, the deviation from Gaussianity seen in the kurtosis of the coefficients of that wavelet [156] cannot be assigned exclusively to those three spots.

[112, 113] have also detected a number of non-Gaussian features, including the cold spot, using the directional wavelets elliptical Mexican hat and Morlet.

All the previous results have been confirmed with the 3-year WMAP CMB map [44] and are expected to be almost unaltered for the 5-year data.

D. Alignment and signed-intensity of local structures

Some of the previous anomalies imply preferred directions in the sky that, under the assumption of Gaussianity, represent deviations from statistical isotropy. Here we describe a different violation of statistical isotropy based on the alignment of CMB structures. The structures are identified by convolving the CMB map with the steerable wavelet formed by the second Gaussian derivative [154]. For each scale and position in the sky the wavelet identifies the orientation which maximizes the absolute value of the wavelet coefficients. Thus this orientation corresponds to the characteristic orientation of the local feature of the signal. The wavelet coefficient in that specific orientation defines the so-called signed-intensity [151]. It should be remarked that these two quantities, local orientation and signed-intensity, are computationally feasible because of the steerability property (see Sec. IV).

Once the local orientation is determined for every position in the sky at a given scale, we can construct the following isotropy test. First, the great circle passing by that position and tangent to the local orientation is identified. Every other pixel which is now crossed by that great circle is considered to be seen by the local orientation of the first position (this procedure is illustrated in Fig. 7), with a weight naturally given by the absolute value of the signed-intensity of the first position. Second, we can assign to each pixel in the sky the total weight given by the sum of the weights of all the pixels which see that pixel. This new total weight signal is even under parity and thus its analysis can be restricted to one hemisphere of reference. The highest total weights represent the positions towards which the CMB features are predominantly directed while the lowest ones represent the positions predominantly avoided by the CMB features. Of course, for an all-sky IGRF all the pixels should have the same total weight on average.

This isotropy test based on the alignment of local orientations has been applied to the first [155] and three-year [151] WMAP data. In both cases a significant violation of isotropy was found at a scale around 10° . The highest total weights (above 3σ) define an axis located very close to the ecliptic one. The highest and the lowest total weights define two planes whose normal axes are close to the CMB dipole one (Fig 8).

Besides the alignment of the local orientations, an analysis of the signed-intensities show three spots at angular scales also around 10° containing a total of 39 $1^\circ.8$ -pixels whose values have a (signal+noise) probability in the 3σ tails (see Fig. 9). This pattern is similar to the one found with the axisymmetric Mexican hat wavelet [150]. The three spots are located in the southern galactic hemisphere confirming the north-south asymmetry. Two of the them are cold, one being identified with the cold spot already detected in [150].

The two anomalies which appear at similar scales, with global significance levels around 1 per cent, are however quite independent.

E. Low variance

Very recently [124] the 1-pdf of the WMAP three-year data has been analysed finding an anomalous low value of the variance as compared to the one expected from the WMAP best-fit cosmological model. The result is even more prominent if only the north ecliptic hemisphere is considered (see Fig. 10), in agreement with the lack of power found in that hemisphere by previous works (see e.g. [59]). The variance of the CMB signal is obtained by fitting the normalized temperature distribution to a Gaussian of zero mean and unit variance. The significance of the result is around 1% (see Fig. 11).

In order to find a possible origin for this anomaly the behaviour of single radiometer and single year data as well as the effect of residual foregrounds and $1/f$ noise have been studied. None of these possibilities can explain the low value of the variance.

Since the largest contribution to the variance comes from the lower multipoles, it is interesting to see if the low quadrupole measured by COBE and WMAP is the cause of the anomalously low variance. Performing the same analysis after subtracting the best-fit quadrupole outside the Kp0 mask the significant of the result is slightly reduced although the variance is still anomalously low.

Beyond the inconsistency found between the best-fit model and the measured variance, one could ask if the latter is consistent with the actual measured power spectrum of the WMAP data. The analysis performed by the same authors show that a strong discrepancy is indeed found. This last result suggests a possible deviation of the CMB data from the IGRF.

F. Cosmological consequences

Given that neither foreground contamination nor known systematics seem to be causing most of the previous anomalies, there has been a number of attempts to explain the cause of the WMAP anomalies by an intrinsic origin. Among them we mention the Rees-Sciama effect produced by large voids [82, 135, 146], inhomogeneous [2, 106] or anisotropic universes [85] and cosmic defects [44]. Although no further evidence has been found for those explanations most of them still remain as plausible. Below we discuss in more detail two interesting possibilities: the Bianchi model and the cosmic texture.

1. Bianchi model

A first interesting attempt to explain the best studied WMAP anomalies was performed by [85, 86] who suggested that such features might be produced by an anisotropic universe, the Bianchi VII_h model. This type of model has a global anisotropic expansion and vorticity that produces geodesic focusing and a spiral pattern in the CMB anisotropy at large angular scales. By fitting the free parameters of that model to the WMAP map the large scale CMB anisotropies produced by its non-standard geometry are determined. After subtracting that pattern from the WMAP data, the best studied WMAP anomalies, namely the low-multipole alignments, the north-south asymmetry and the cold spot, were significantly reduced.

This result seemed to suggest that the universe was not well represented by the homogeneous and isotropic FLRW model and that a perturbation in the form of a Bianchi VII_h was a better representation. However, a more detailed examination of the best-fitted parameters of the Bianchi model when a dark energy was included showed values of the dark energy and matter energy density far from the ones measured by many current cosmological tests [24, 87].

Considering other Bianchi models with vorticity and shear, like the Bianchi IX with a closed geometry, do not help since they do not exhibit geodesic focusing or the spiral pattern.

Very recently, [25] computed the Bayesian evidence of the Bianchi template when the cold spot was not included in the analysis (see below for an alternative interpretation of the cold spot). The result was that the evidence was now significantly reduced, reinforcing the idea that the cold spot was likely to be driving any Bianchi VII_h detection.

2. The cold spot texture

Recently, [44] performed a Bayesian evidence analysis to test the hypothesis that the cold spot is produced by a cosmic texture. This is a type of topological defect that, as explained in Sec. III B 2, in the standard theories of unification of the fundamental forces of nature, are expected to appear in the early universe. The motivation for considering a texture as the origin of the cold spot is its typical spherical anisotropy pattern left in the CMB and the relatively small number of spots expected at scales of several degrees (see Fig. 12).

The hypothesis test considered consisted in the comparison of the following two hypotheses: the null hypothesis H_0 for which the cold spot is just a rare fluctuation of the IGRF predicted by the standard inflationary model, and the alternative hypothesis, H_1 for which on top of the inflationary Gaussian CMB fluctuations there are non-Gaussian ones as produced by the texture model. The test is applied to a circular area of 40° diameter centered on the cold spot position. The posterior probability ratio of the two hypotheses is:

$$\rho = \frac{Pr(H_1|\mathbf{D})}{Pr(H_0|\mathbf{D})} = \frac{E_1 Pr(H_1)}{E_0 Pr(H_0)} , \quad (31)$$

where \mathbf{D} is the data vector, and E_i the evidence which is the average likelihood L with respect to the priors $\Pi(\Theta_i)$ in the parameters Θ_i of the hypothesis H_i ,

$$E_i = Pr(\mathbf{D}|H_i) = \int L_i(\Theta_i|H_i)\Pi(\Theta_i)d\Theta_i , \quad (32)$$

and $Pr(H_i)$ is the a priori probability of hypothesis H_i . The a priori probability ratio is usually set to unit for lack of information, but since in our case the analysis is centered in the cold spot (an a posteriori selected pixel) it should be given by the sky fraction f_s covered by textures. Given that a scale-invariant distribution of spots is expected and considering only textures above 1° (photon diffusion would smear out textures smaller than that) $f_s = 0.017$. The likelihood function is simply $L \propto (-\chi^2/2)$ where $\chi^2 = (\mathbf{D} - \mathbf{T})'\mathbf{N}^{-1}(\mathbf{D} - \mathbf{T})$ and \mathbf{N} is the CMB+noise covariance matrix. The anisotropy pattern T produced by a texture can be approximated by an analytical spherical profile [149] with only two free parameters: the amplitude which is related to the fundamental symmetry-breaking energy scale, and the angular scale which is related to the redshift when the texture unwinds.

The result of the analysis is a probability ratio $\rho = 2.5$ for the three-year WMAP data, favouring the texture hypothesis (see Fig 13 for the resulting best-fit texture template). This result is slightly increased ($\rho = 2.7$) for the five-year data due to the reduction in the noise amplitude. The texture interpretation helps to alleviate the excess found in the kurtosis, being at the same time compatible with the observed abundance, shape, size and amplitude of the spot. In particular, the symmetry-breaking scale inferred from this analysis, $\phi_0 \approx 8.7 \times 10^{15}$ GeV, is compatible with the upper limit obtained from the CMB power spectrum analysis [21].

More recently, [45] have extended the Bayesian evidence analysis to models based on the Rees-Sciama effect produced by voids or on the SZ effect. The result is that, contrary to the texture model, no positive evidence is found for those models.

VII. CONCLUDING REMARKS AND FUTURE PERSPECTIVES

The main conclusion derived from the large amount of analyses, involving a variety of methods, performed to test the Gaussianity of the CMB anisotropies, specially those measured by WMAP, is that the standard IGRF prediction is a good representation of their properties as a first approach. Furthermore, a number of significant deviations from the ideal IGRF has also been reported whose origin and interpretation is still under debate. Some of them might have to do with foreground residuals or unknown systematics while others could be a hint of new physics with profound implications for our understanding of the universe. Probably, to answer those questions we will have to wait for new data coming from the advanced experiments being built and expected to be operative in the next years.

Future experiments will shed light on the open questions remaining from the up-to-date analyses of the CMB data, specially on the WMAP anomalies discussed in Sec. VI. In particular, the Planck mission is expected to provide

all-sky, high quality, multifrequency maps in the frequency range 30 – 900GHz. The wider frequency range and the higher sensitivity and resolution will allow an improvement in the quality of the resulting CMB map. As a consequence, an improvement in the control of the foreground emission is expected as well as a reduction in the sky area required to be masked. In addition to the temperature, improvements are also expected in the polarization maps which will be provided by Planck, meaning an important complement for probing the nature of the anomalies as well as for testing the different physical interpretations proposed for them. Missions for measuring polarization at the highest sensitivity allowed by present technology, and with the main aim of probing the existence of the gravitational wave background, have been recently proposed to both agencies, ESA and NASA. As for the temperature, the linear polarization expected to be produced as a consequence of the standard inflationary period of the universe also possesses properties very close to those of the IGRF studied in Sec. II. Therefore, extensions of the methods already discussed in Sec IV for temperature are also expected to be applied to test the Gaussianity of the future polarization maps.

Acknowledgements

I thank R.B. Barreiro and P. Vielva for useful comments on the manuscript and M. Cruz, A. Curto and C. Monteserín for helping me with some figures. I acknowledge financial support from the Spanish MEC project ESP2007-68058-C03-02. I also acknowledge the use of LAMBDA, support for which is provided by the NASA Office of Space Science. The work has also used the software package HEALPix (<http://www.eso.org/science/healpix>) developed by K.M. Gorski, E.F. Hivon, B.D. Wandelt, J. Banday, F.K. Hansen and M. Barthelmann [68].

-
- [1] Adler, R. J., 1981, *The geometry of random fields*, John Wiley & Sons, Chichester
 - [2] Adler R.J., Bjorken J.D. & Overduin J.M., 2006, gr-qc/0602102
 - [3] Ademan-McCarthy J.K. et al., 2008, ApJS, 175, 297
 - [4] Aghanim N., Desert F.X., Puget J.L. & Gispert R., 1996, A&A, 311, 1.
 - [5] Aghanim N. & Puget J.L., 2006, in CMB and Physics of the early Universe, ed. G. de Zotti et al., Proceeding of Science
 - [6] Antoine J.-P. & Vanderheynt P., 1998, J. Math. Phys. 39, 3987
 - [7] Barreiro R.B., Sanz J.L., Martínez-González E., Cayón L. & Silk J., 1997, ApJ, 478, 1
 - [8] Barreiro R.B., 2007, in Highlights of Spanish Astrophysics IV. Proceedings of the VII Scientific Meeting of the Spanish Astronomical Society (SEA), Barcelona, September 12-15, 2006. Ed. F. Figuras et al., Springer
 - [9] Barreiro R.B., 2008, in Data Analysis in Cosmology, eds. V.J. Martínez et al., Springer
 - [10] Barrow J.D., Juszkiewicz R. & Sonoda D.H., 1985, MNRAS, 213, 917
 - [11] Barrow J.D., Ferreira P.G. & Silk J., 1997, Phys. Rev. Lett., 78, 3610
 - [12] Bartelmann M. & Schneider P., 2001, Phys. Rep. 340, 291
 - [13] Bartolo N., Komatsu E., Matarrese S. & Riotto A., 2004, Phys. Rep., 402, 103
 - [14] Bartosz L., 2008, A&A, submitted, astro-ph/08031409
 - [15] Bassler P.J. & Pierpaoli C., 1996, J. Magn. Reson. Med. B, 111, 209-219
 - [16] Bennett C.L. et al., 1994, ApJ, 436, 443
 - [17] Bennett C.L. et al., 2003, ApJS, 148, 1
 - [18] Bennett C.L. et al., 2003, ApJS, 148, 97
 - [19] Bernui A., Villela T., Wuensche C.A., Leonardi R. & Ferreira I., A&A, 454, 409
 - [20] Bernui A., Mota B., Reboucas M.J. & Tavakol R., A&A, 464, 479
 - [21] Bevis N., Hindmarsh M. & Kunz M., 2004, Phys. Rev. D, 70, 043508
 - [22] Bielewicz P., Eriksen H.K., Banday A.J., Górski K.M. & Lilje P.B., 2005, ApJ, 635, 750
 - [23] Bond J.R. & Efstathiou G., 1987, MNRAS, 226, 655
 - [24] Bridges M., McEwen J.D., Lasenby A.N. & Hobson M.P., 2007, MNRAS, 377, 1473
 - [25] Bridges M., McEwen J.D., Cruz M., Hobson M.P., Lasenby A.N., Vielva P. & Martínez-González, 2007, MNRAS, submitted, astro-ph/07121789
 - [26] Buchbinder E., Khoury J. & Ovrut B.A., 2007, hep-th/07105172
 - [27] Bunn, E.F., Ferreira, P. & Silk, J. 1996, Phys. Rev. Lett., 77, 2883
 - [28] Cabella P. et al., 2006, MNRAS, 369, 819
 - [29] Cayón L., Martínez-González E. & Sanz J.L., 1991, MNRAS, 253, 599
 - [30] Cayón L. et al., 2001, MNRAS, 326, 1243
 - [31] Cayón L., Martínez-González E., Argüeso F., Banday A.J., Gorski K.M., 2003, MNRAS, 339, 1189
 - [32] Cayón L., Jin J. & Treaster A., 2005, MNRAS, 362, 826
 - [33] Chen G. et al., 2004, ApJ, 611, 655
 - [34] Chen G. & Szapudi I., 2005, ApJ, 635, 743
 - [35] Chiang L.-Y., Naselsky P.D., Verkhodanov O.V. & Way M.J., 2003, ApJL, 590, 65
 - [36] Colless M.M. et al., 2001, MNRAS, 328, 1039

- [37] Copi C.J., Huterer D. & Starkman G.D., 2004, *Phys. Rev. D*, 70, 043515, astro-ph/0310511
- [38] Copi C.J., Huterer D., Schwarz D. & Starkman G.D., 2007, *Phys. Rev. D*, 75, 023507
- [39] Cornish N.J., Spergel D.N., Starkman, G.D. & Komatsu E., 2004, *Phys. Rev. Lett.*, 92, 201302
- [40] Creminelli P., Nicolis A., Senatore L., Tegmark M. & Zaldarriaga M., 2006, *JCAP*, 0605, 004
- [41] Cresswell J.G., Liddle A.R., Mukherjee P. & Riazuelo A., 2006, *Phys. Rev. D*, 73, 041302, astro-ph/0512017
- [42] Cruz M., Martínez-González E., Vielva P. & Cayón L., 2005, *MNRAS*, 356, 29
- [43] Cruz M., Tucci M., Martínez-González E. & Vielva P., 2006, *MNRAS*, 369, 57
- [44] Cruz M., Turok N., Vielva P., Martínez-González E. & Hobson M., 2007, *Science*, 318, 1612
- [45] Cruz M., Martínez-González E., Vielva P., Diego J.M., Hobson M.P. & Turok N., 2008, *MNRAS*, submitted, astro-ph/08042904
- [46] Curto A. et al., 2007, *A&A*, 474, 23
- [47] Curto A. et al., 2008, *A&A*, submitted, astro-ph/08040136
- [48] de Oliveira-Costa A., Smoot G.F. & Starobinsky A.A., 1996, *ApJ*, 468, 457
- [49] de Oliveira-Costa A., Tegmark M., Zaldarriaga M. & Hamilton A., 2004, *Phys. Rev. D*, 69, 063516
- [50] de Oliveira-Costa A. & Tegmark M., 2006, *Phys. Rev. D*, 74, 023005
- [51] De Troia G. et al., 2007, *ApJL*, 670, 73
- [52] Delabrouille J. & Cardoso J.F., 2008, in *Data Analysis in Cosmology*, eds. V.J. Martínez et al., Springer
- [53] Davies R., in this volume
- [54] Donoghue E.P. & Donoghue J.F., 2005, *Phys. Rev. D*, 71, 043002
- [55] Doré O., Colombi S. & Bouchet F.R., 2003, *MNRAS*, 344, 905
- [56] Delabrouille J. & Cardoso J.F., 2008, in *Data Analysis in Cosmology*, eds. V.J. Martínez et al., Springer
- [57] Durrer R., Kahniashvili T. & Yates A., 1998, *Phys. Rev. D*, 58, 123004
- [58] Durrer R., 2007, *New Astronomy Reviews*, 51, 257
- [59] Eriksen H.K., Hansen F.K., Banday A.J., Gorski K.M. & Lilje P.B., 2004, *ApJ*, 605, 14
- [60] Eriksen H.K., Novikov D.I., Lilje P.B., Banday A.J., Gorski K.M., 2004, *ApJ*, 612, 64
- [61] Eriksen H.K., Banday A.J., Gorski K.M. & Lilje P.B., 2005, *ApJ*, 622, 58
- [62] Eriksen H.K., Banday A.J., Gorski K.M., Hansen F.K. & Lilje P.B., 2007, *ApJL*, 660, L81
- [63] Freeman, P.E., Genovese, C.R., Miller, C.J., Nichol, R.C. & Wasserman, L., 2006, *ApJ*, 638, 1
- [64] Gaztañaga E. & Wagg J., 2003, *Phys. Rev. D*, 68, 021302
- [65] Génova-Santos R. et al., 2005, *MNRAS*, 363, 79
- [66] Génova-Santos R. et al., 2008, *MNRAS*, submitted, astro-ph/08040199
- [67] Giovannini M., 2004, *Int. J. Mod. Phys. D*, 13, 391
- [68] Górski K.M., Hivon E.F., Wandelt B.D., Banday J., Hansen F.K. & Barthelmann M., 2005, *ApJ*, 622, 759
- [69] Hajian A., Souradeep T. & Cornish N., 2005, *ApJ*, 618, 63
- [70] Hajian A. & Souradeep T., 2006, *Phys. Rev. D*, 74, 123521
- [71] Han J. & Wielebinski R., 2002, *ChJA&A*, 2, 293
- [72] Hansen F.K., Banday A.J. & Gorski K.M., 2004, *MNRAS*, 354, 641
- [73] Hansen F.K., Cabella P., Marinucci D. & Vittorio N., 2004, *ApJ*, 607, L67
- [74] Hikage C., Komatsu E. & Matsubara T., 2006, *ApJ*, 653, 11
- [75] Hikage C., Matsubara T., Coles P., Liguori M., Hansen F.K. & Matarrese S., 2008, *MNRAS*, submitted, astro-ph/08023677
- [76] Hinshaw G. et al., 2007, *ApJS*, 170, 288
- [77] Hinshaw G., et al., 2008, *ApJS*, submitted, astro-ph/08030732
- [78] Huang M.-X. & Shiu G., 2006, *Phys. Rev. D*, 74, 121301
- [79] Hu W., 2000, *Phys. Rev. D*, 62, 043007
- [80] Hu W., 2001, *Phys. Rev. D*, 64, 083005
- [81] Hu W. and Dodelson S., 2002, *ARAA*, 40, 171
- [82] Inoue K.T. & Silk J., 2007, *ApJ*, 664, 650
- [83] Inoue K.T. & Sugiyama N., 2003, *Phys. Rev. D*, 67, 043003
- [84] Inoue K.T. & Silk J., 2007, *ApJ*, 664, 650
- [85] Jaffe T.R., Banday A.J., Eriksen H.K., Gorski K.M. & Hansen F.K., 2005, *ApJL*, 629, L1
- [86] Jaffe T.R., Banday A.J., Eriksen H.K., Gorski K.M. & Hansen F.K., 2006, *A&A*, 460, 393
- [87] Jaffe T.R., Hervik S., Banday A.J., Gorski K.M., 2006, *ApJ*, 644, 701
- [88] Jones B.J.T., 2008, in *Data Analysis in Cosmology*, eds. V.J. Martínez et al., Springer
- [89] Kaiser N. & Stebbins A., 1984, *Nature*, 310, 391
- [90] Katz G. & Weeks J., 2004, *Phys. Rev. D*, 70, 063527
- [91] Khoury J., Ovrut B.A., Steinhardt P.J. & Turok N., *Phys. Rev. D*, 2001, 64, 123522
- [92] Kibble T.W.B., 1976, *J. Phys. A*, 9, 1387
- [93] Kogut A., Hinshaw G. & Banday A.J., 1997, *Phys. Rev. D*, 55, 1901
- [94] Komatsu E., 2001, Ph.D. thesis, astro-ph/0206039
- [95] Komatsu E. & Spergel D.N., 2001, *Phys. Rev. D*, 63, 063002
- [96] Komatsu E., Wandelt B.D., Spergel D.N., Banday A.J. & Gorski K.M., 2002, *ApJ*, 566, 19
- [97] Komatsu E. et al., 2003, *ApJS*, 148, 119
- [98] Komatsu E., Spergel D.N. & Wandelt B.D., 2005, *ApJ*, 634, 14
- [99] Komatsu E. et al., 2008, *ApJS*, submitted, astro-ph/08030547

- [100] Kronberg P.P., 2004, JKAS, 37, 501
- [101] Kunz M., Aghanim N., Cayón L., Forni O., Riazuelo A. & Uzan J.P., 2006, Phys. Rev. D, 73, 023511
- [102] Kunz M., Aghanim N., Riazuelo A. & Forni O., 2008, Phys. Rev. D, 77, 023525
- [103] Lachièze-Rey, M. & Luminet, J.-P. 1995, Phys. Rep., 254, 135
- [104] Land K. & Magueijo J., 2005, Phys. Rev. Lett., 95, 071301
- [105] Land K. & Magueijo J., 2005, MNRAS, 357, 994
- [106] Land K. & Magueijo J., 2006, MNRAS, 367, 1714
- [107] Land K. & Magueijo J., 2007, MNRAS, 378, 153
- [108] Levin J., 2002, Phys. Rep., 365, 251-333
- [109] Lewis A., 2004, Phys. Rev. D, 70, 043011
- [110] Longuet-Higgins, M. S., 1957, Phil. Trans. Roy. Soc. London, A, 249, 321
- [111] Luminet J.-P., Weeks J.R., Riazuelo A., Lehoucq R. & Uzan J.-P., 2003, Nature, 425, 593
- [112] McEwen J.D., Hobson M.P., Lasenby A.N. & Mortlock D.J., 2005, MNRAS, 359, 1583
- [113] McEwen J.D., Hobson M.P., Lasenby A.N. & Mortlock D.J., 2005, MNRAS, submitted, astro-ph/08032157
- [114] Martínez-González E., Sanz J.L. & Silk J., 1990, ApJL, 335, L5
- [115] Martínez-González E. & Sanz J.L., 1990, MNRAS, 247, 473
- [116] Martínez-González E. & Sanz, J.L. 1995, A&A, 300, 346
- [117] Martínez-González E., Sanz J.L. & Cayón L., 1997, ApJ, 484, 1
- [118] Martínez-González E., Gallegos J.E., Argüeso F., Cayón L., Sanz J.L., 2002, MNRAS, 336, 22
- [119] Martínez-González E., 2008, in Data Analysis in Cosmology, eds. V.J. Martínez et al., Springer
- [120] Matarrese S., in this volume
- [121] Mollerach S., Gangui A., Luchin F., Matarrese S., 1995, ApJ, 453, 1
- [122] Monteserín C., Barreiro R.B., Sanz, J.L. & Martínez-González E., 2005, MNRAS, 360, 9
- [123] Monteserín C., Barreiro R.B., Martínez-González E. & Sanz J.L., 2006, MNRAS, 371, 312
- [124] Monteserín C., Barreiro R.B., Vielva P., Martínez-González E., Hobson M.P. & Lasenby A.N., 2007, MNRAS, accepted, astro-ph/07064289
- [125] Mukherjee P. & Wang Y., 2004, ApJ, 613, 51
- [126] Niarchou A. & Jaffe A., 2007, Phys. Rev. Lett., 99, 081302
- [127] Ostriker J.P. & Vishniac E.T., 1986, ApJ, 306, 510
- [128] Park C.-G., 2004, MNRAS, 349, 313
- [129] Partridge B., in this volume
- [130] Phillips N.G. & Kogut A., 2006, ApJ, 645, 820
- [131] Rees M.J. & Sciama D.W., 1968, Nature, 517, 611
- [132] Rocha G., Cayón L., Bowen R., Canavezes A., Silk J., Banday A.J. & Gorski K.M., 2004, MNRAS, 351, 769, astro-ph/0205155
- [133] Roukema, B., 2000, MNRAS, 312, 712
- [134] Rubiño-Martín J.A. et al, 2006, MNRAS, 369, 909
- [135] Rudnick L., Brown S. & Williams L.R., 2007, ApJ, 671, 40
- [136] Sachs R. K. & Wolfe A. M., 1967, ApJ, 147, 73
- [137] Sanz J.L., Martínez-González E., Cayón L., Silk, J. & Sugiyama N., 1996, ApJ, 467, 485
- [138] Schmalzing J. & Gorski K.M., 1998, MNRAS, 297, 355
- [139] Seljak U., 1996, ApJ, 463, 1
- [140] Smith S. et al., 2004, MNRAS, 352, 887
- [141] Smoot G. F. et al., 1992, ApJL, 396, L1
- [142] Spergel D. N. et al., 2007, ApJS, 170, 377
- [143] Schwartz D.J., Starkman, G.D., Huterer D. & Copi C.J., 2004, Phys. Rev. Lett., 93, 1301
- [144] Sunyaev R.A. & Zeldovich Y.B., 1972, Comm. Astrophys. Space Phys., 4, 173
- [145] Tegmark M., de Oliveria-Costa A., Hamilton A.J., 2003, Phys. Rev. D, 68, 123523
- [146] Tomita K., 2005, Phys. Rev. D, 72, 103506
- [147] Turok N., 1989, Phys. Rev. Lett., 63, 2625
- [148] Turok N. & Spergel D., 1990, Phys. Rev. D, 64, 2736
- [149] Vilenkin A. & Shellard E.P.S., 1994, *Cosmic Strings and Other Topological Defects*, Cambridge University Press
- [150] Vielva P., Martínez-González E., Barreiro R.B., Sanz J.L. & Cayón L., 2004, ApJ, 609, 22
- [151] Vielva P., Wiaux Y., Martínez-González E. & Vanderheynt P., 2007, MNRAS, 381, 932
- [152] Vielva P., 2007, in Wavelets XII. Proceedings of the SPIE, ed. D. Van De Ville et al., 6701, 670119
- [153] Vishniac E.T., 1986, ApJ, 322, 597
- [154] Wiaux Y., Jacques L. & Vanderheynt P., 2005, ApJ, 632, 5
- [155] Wiaux Y., Vielva P., Martínez-González E. & Vanderheynt P., 2006, Phys. Rev. Lett., 96, 151303
- [156] Wiaux Y., Vielva P., Barreiro R.B., Martínez-González E. & Vanderheynt P., 2008, MNRAS, 385, 939
- [157] Yadav A.P.S., Komatsu E., Wandelt B.D., 2007, ApJ, 664, 680
- [158] Yadav A.P.S., Komatsu E., Wandelt B.D., Liguori M., Hansen F.K. & Matarrese S., 2007, ApJ, submitted, astro-ph/07114933

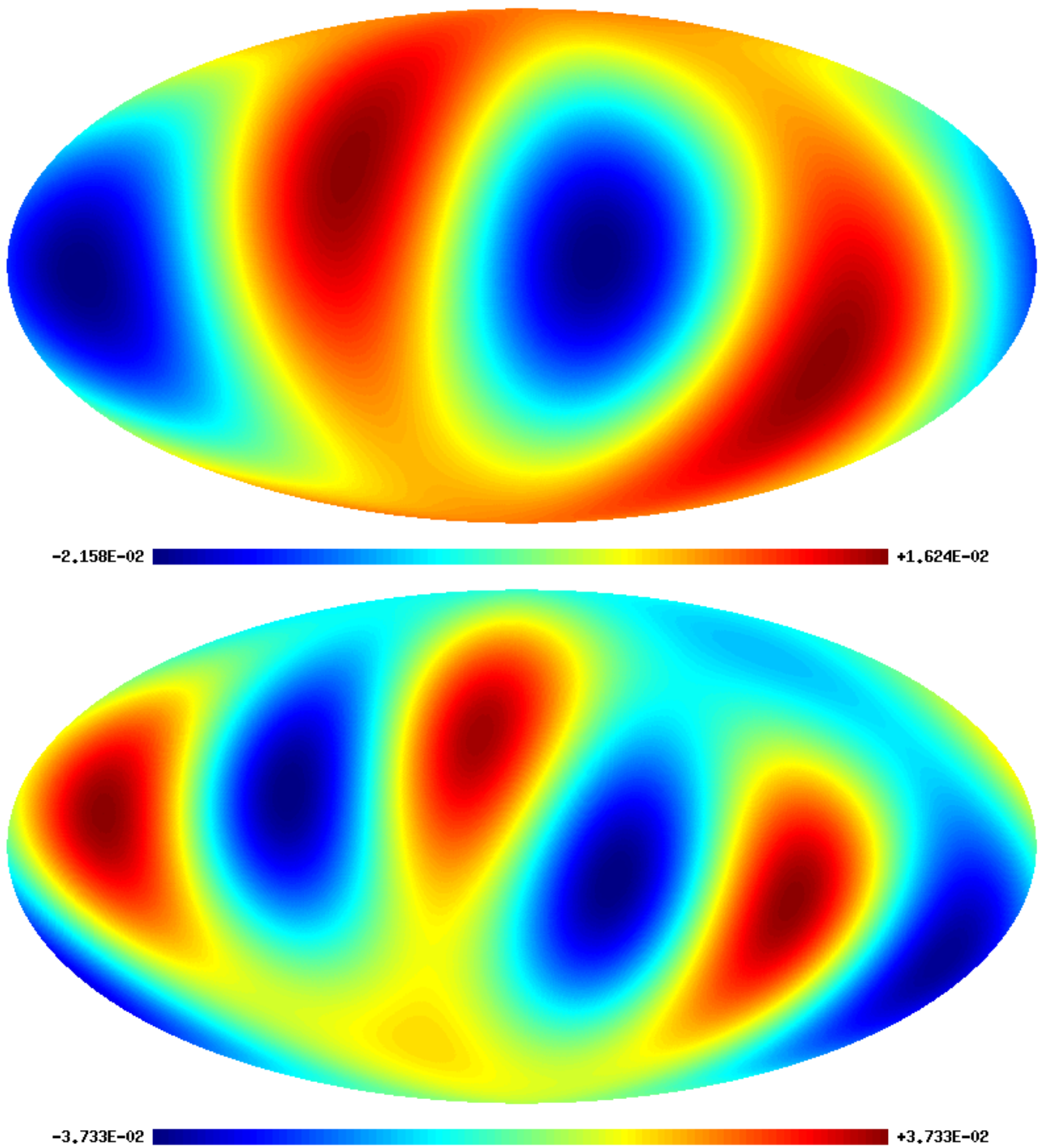


FIG. 5: Maps of the quadrupole and octopole obtained from the WMAP 5-years ILC map. The ILC map can be obtained from the LAMBDA web page (<http://lambda.gsfc.nasa.gov/>).

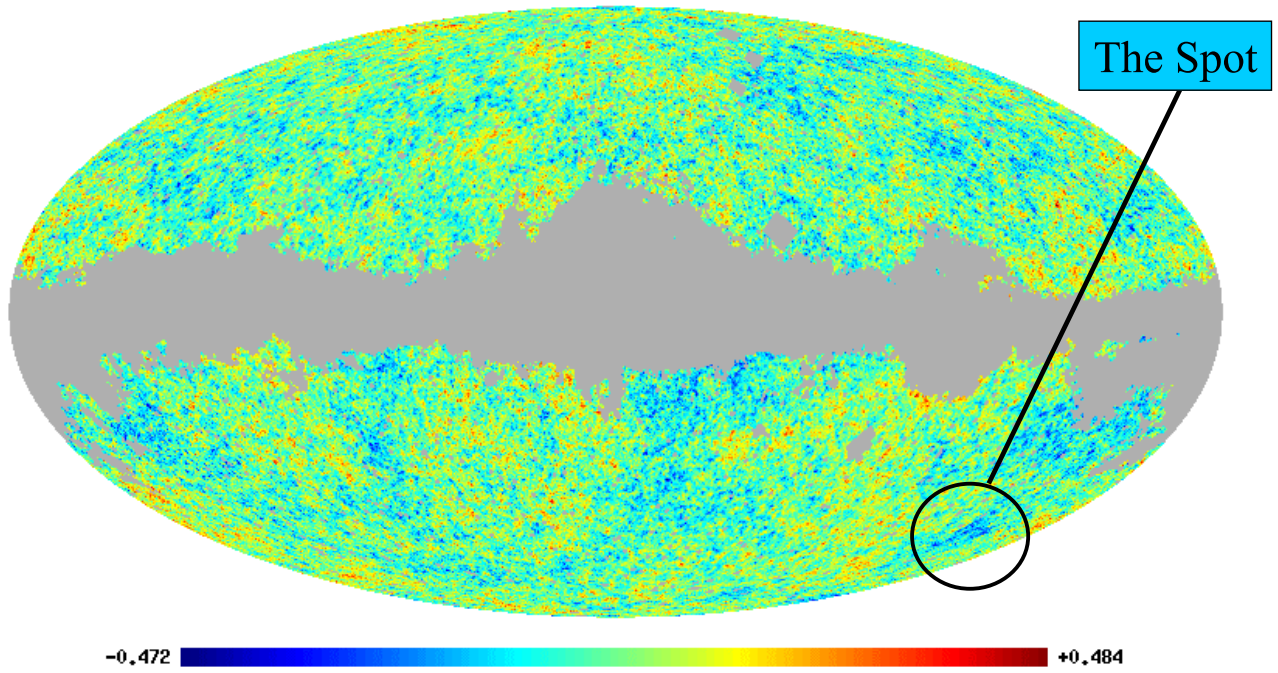


FIG. 6: The cold spot in the 5-years WMAP combined map. This map is a noise-weighted combination of the V and W maps given in [77] where the pixels contaminated by Galactic or extragalactic foregrounds have been masked with the KQ75 mask. The WMAP maps and masks can be found in the LAMBDA web page.

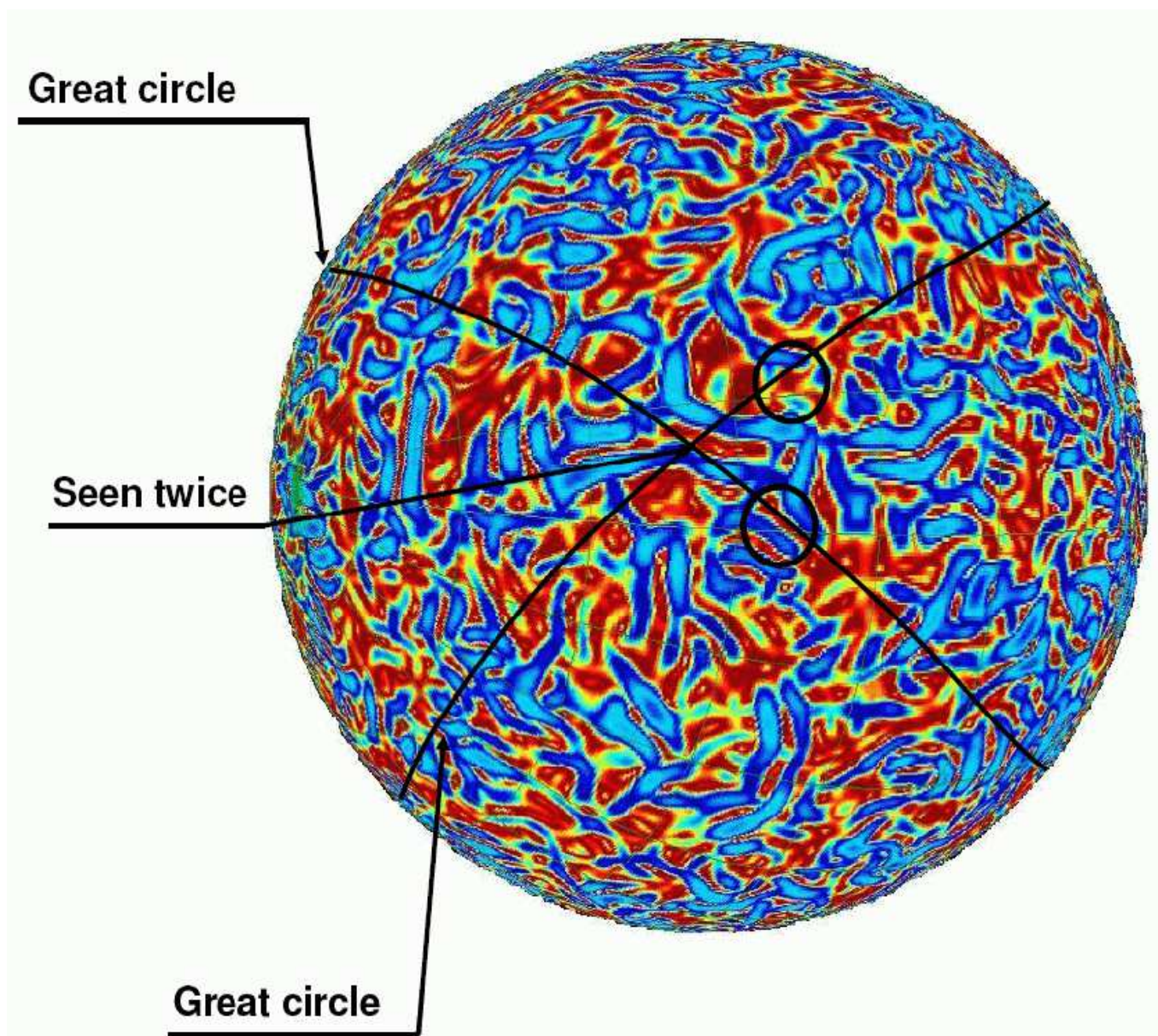


FIG. 7: A simulated map of the signed-intensity where the great circles corresponding to two local features are shown. All the pixels crossed by each great circle are considered to be seen by the corresponding local feature. The position which is crossed by both great circles is thus said to be seen twice. See [151] for more details.

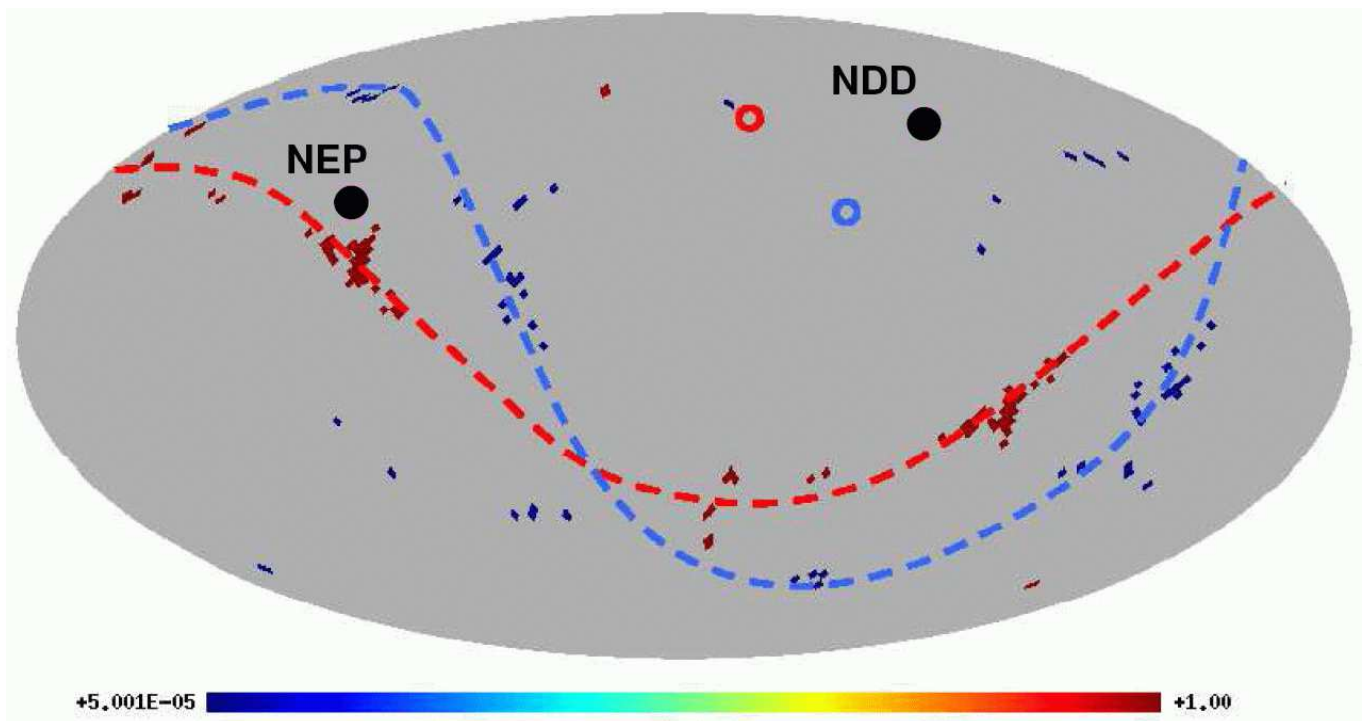


FIG. 8: The highest (lowest) total weights above (below) 3σ are plotted in red (blue). A cluster of positive total weights can be seen close to the NEP. The red (blue) dashed line is the best fit plane to the highest (lowest) total weights. The normal axes defined by both planes point towards directions close to the northern direction of the dipole NDD. From [151].

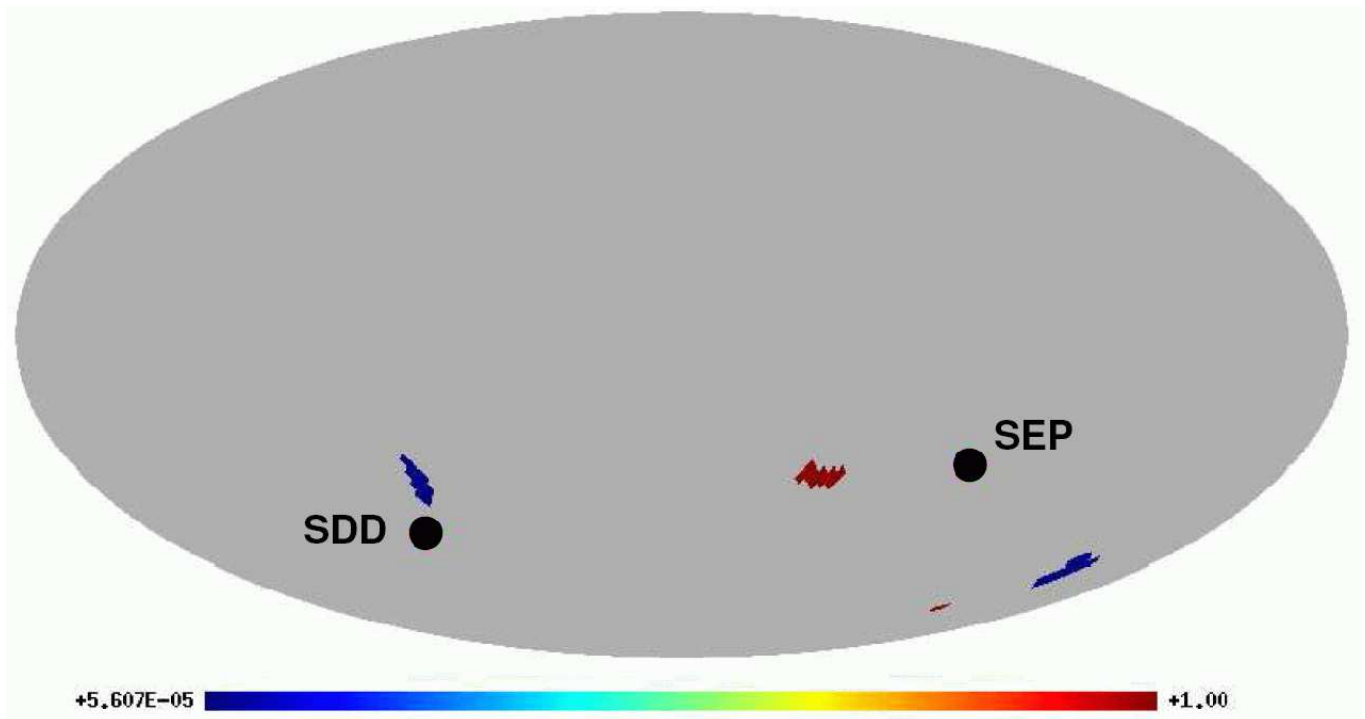


FIG. 9: Map of signed-intensities with probability in the 3σ tails. In blue are the pixels with negative values and in red the positive ones. The signed-intensities are grouped around three clusters, one formed by the negative values and other two by the positive ones. Also shown are the positions of the South ecliptic pole (SEP) and the southern direction of the CMB dipole (SDD). From [151].

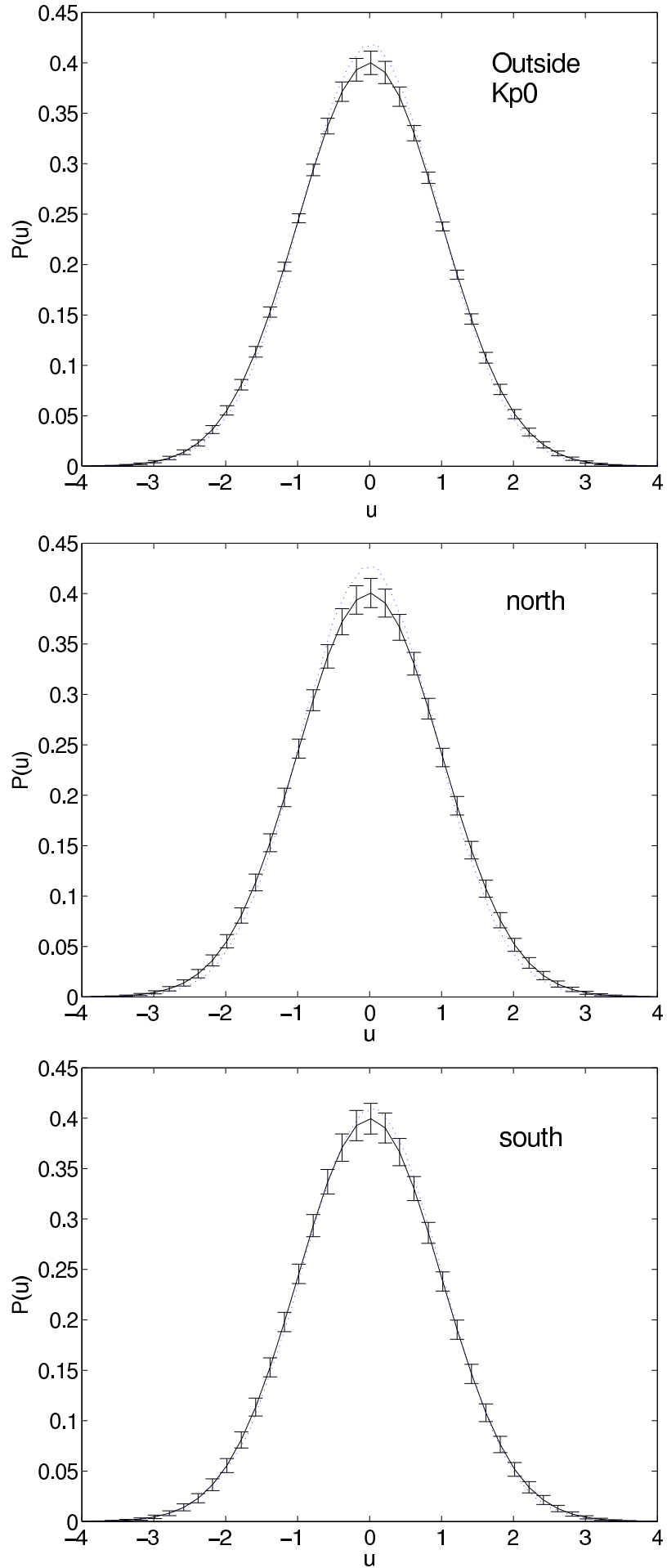


FIG. 10. The distribution of the normalized HMAP data with the $Kp=0$ and (dotted line) is a normal distribution.

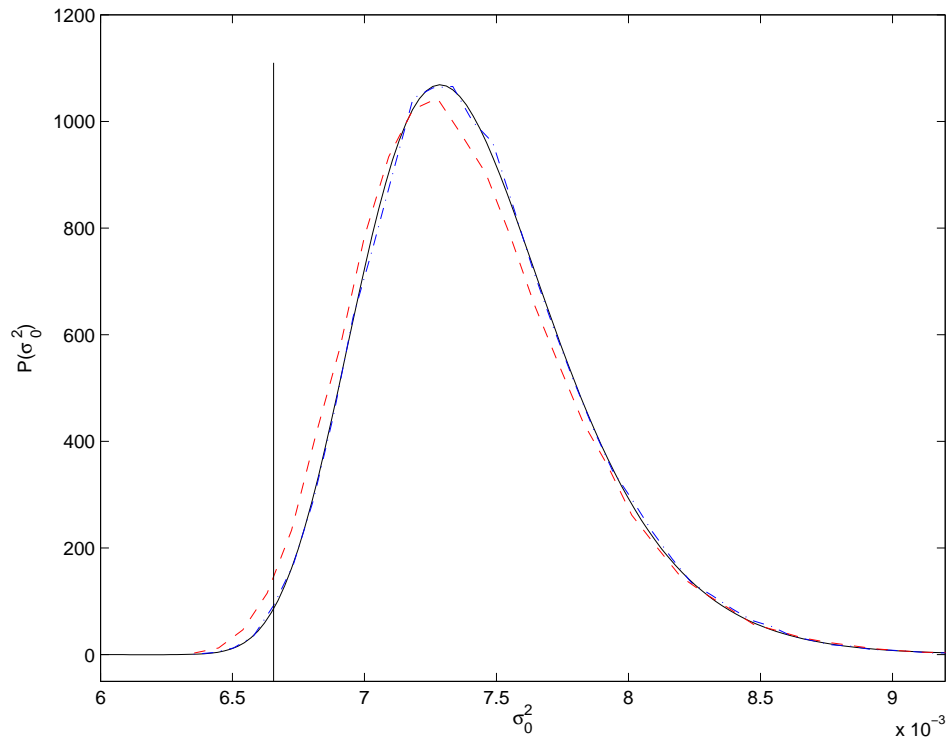


FIG. 11: Theoretical pdf of the CMB variance (calculated following [29], solid line) compared to the averaged pdf obtained from 60000 Gaussian simulations of the WMAP best-fit model over the whole sky (blue dot-dashed line) and using only the pixels outside the Kp0 mask (red dashed line). The solid vertical line indicates the value obtained from the 3-year WMAP data. See [124] for more details.

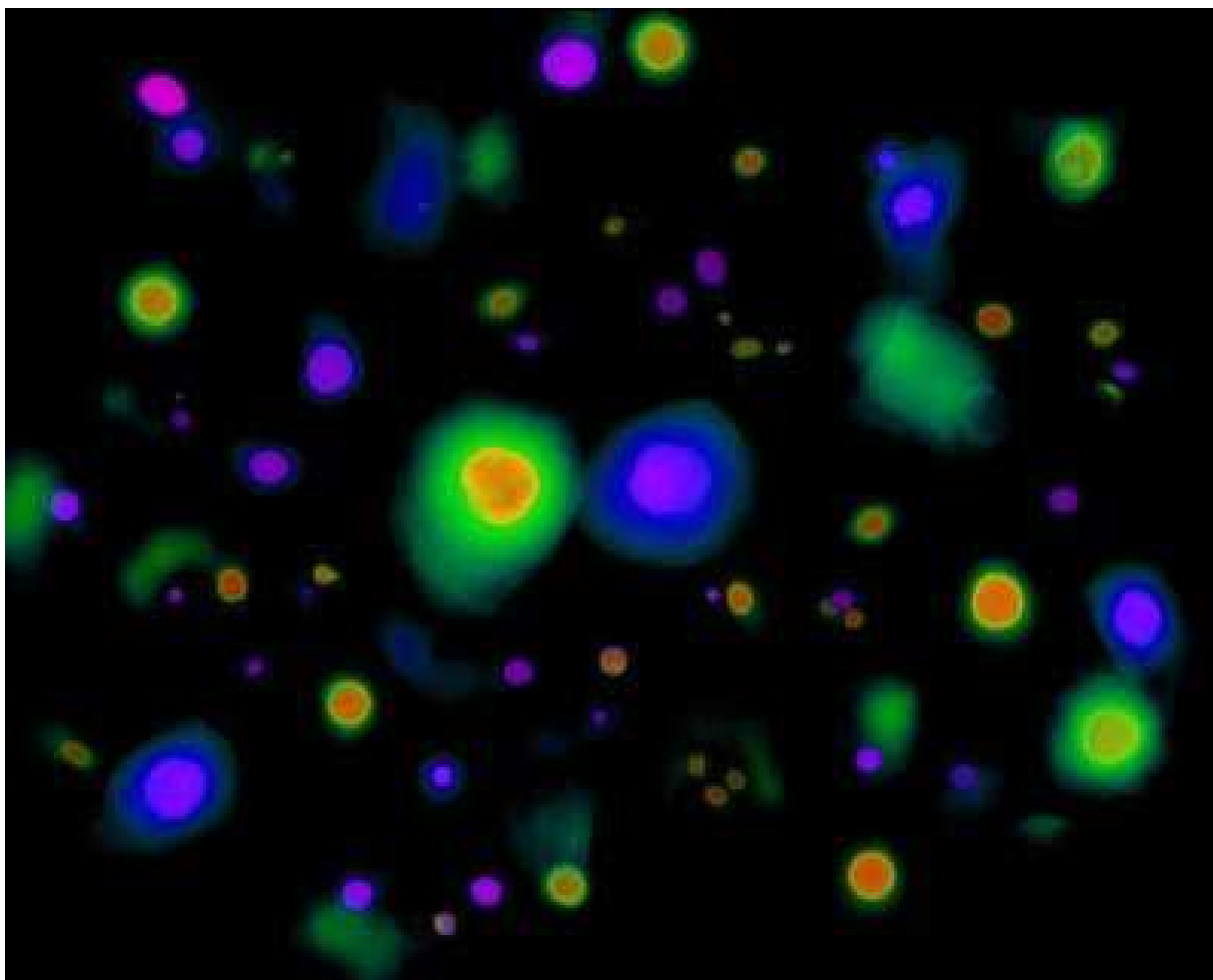


FIG. 12: Image of the high resolution texture simulation performed by N. Turok and V. Travieso and available at (<http://www.damtp.cam.ac.uk/cosmos/viz/movies/neil.html>). The distribution of texture spots on the sky is predicted to be scale-invariant.

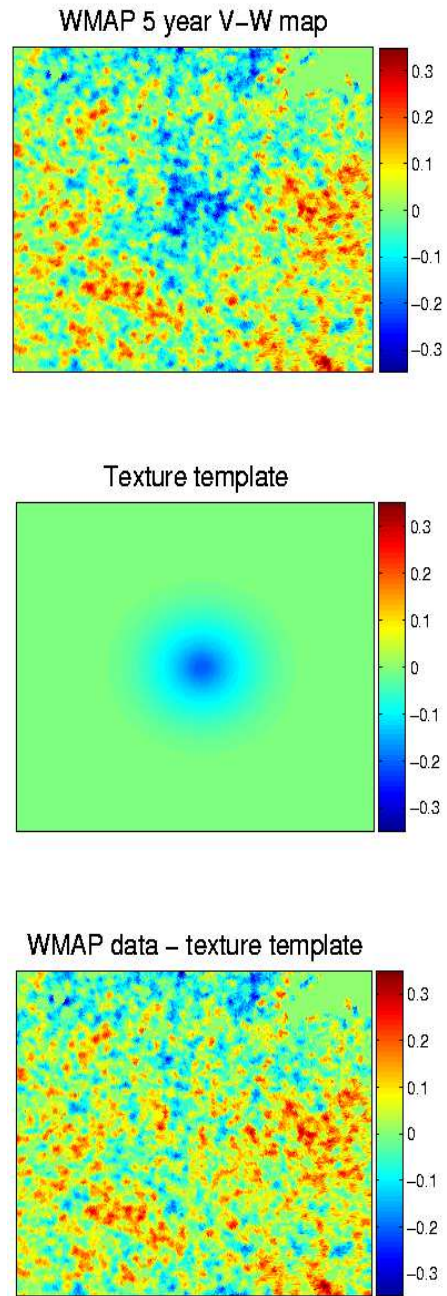


FIG. 13: A $43^\circ \times 43^\circ$ patch centered at Galactic coordinates $(-57^\circ, 209^\circ)$ and obtained from the 5-year WMAP combined map given in Fig. 6, is shown in the top panel. The best fit texture template is in the middle and the result of subtracting it from the WMAP map in the bottom. The units shown in the colorbars are mK . See [44] for more details.